Journal Pre-proofs

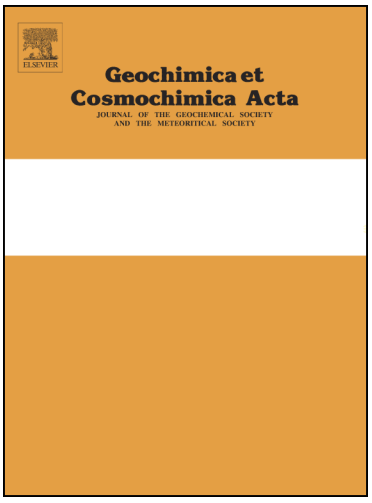

Experimental constraints on siderite clumped isotope thermometry

Ella A. Holme, Gregory A. Henkes, Nicholas J. Tosca, Troy E. Rasbury, Jordan M. Young, Douglas R. Schaub, Hanna Nekvasil, Joel A. Hurowitz

PII: S0016-7037(22)00657-3
DOI: https://doi.org/10.1016/j.gca.2022.12.012
Reference: GCA 12902

To appear in: *Geochimica et Cosmochimica Acta*

Received Date: 7 March 2022
Accepted Date: 8 December 2022

Please cite this article as: Holme, E.A., Henkes, G.A., Tosca, N.J., Rasbury, T.E., Young, J.M., Schaub, D.R., Nekvasil, H., Hurowitz, J.A., Experimental constraints on siderite clumped isotope thermometry, *Geochimica et Cosmochimica Acta* (2022), doi: https://doi.org/10.1016/j.gca.2022.12.012

Experimental constraints on siderite clumped isotope thermometry

Ella A. Holme[*,a,1], Gregory A. Henkes[a], Nicholas J. Tosca[b], Troy E. Rasbury[a], Jordan M. Young[a], Douglas R. Schaub[a], Hanna Nekvasil[a], Joel A. Hurowitz[a]

[a]*Department of Geosciences, Stony Brook University, Stony Brook, NY 11794, USA*

[b]*Department of Earth Sciences, University of Cambridge, CB2 3EQ, England, UK*

[1]*Department of Earth & Planetary Sciences, Yale University, New Haven, CT 06511, USA*

Abstract

We present results from chemostatic siderite precipitation experiments conducted using a modified constant composition method at temperatures between 15-75 °C and compare these results with previous temperature relationships to obtain a composite low temperature relationship for siderite clumped isotope ratios (Δ_{47}) from 8.5-75°C:

$$\Delta_{47} = 0.0364(\pm 0.004) * \frac{10^6}{T^2} + 0.1672(\pm 0.046)[\pm 95\%\ CL],\ R^2 = 0.708$$

The slope of this line is statistically indistinguishable from those reported for aragonite, calcite, and dolomite clumped isotopes, but differs in its intercept. To test whether this difference results from mineralogical differences in phosphoric acid fractionation factors (AFF) between siderite and Ca-Mg carbonates, we heated siderite to 625°C at 1 GPa, which yielded a statistically indistinguishable Δ_{47} value from that predicted by published clumped isotope calibrations populated by Ca-and Mg-carbonate data at higher temperatures. Thus, the apparent difference between siderite clumped isotope behavior and that of other carbonate minerals may not be well explained by differences in AFF. Despite differences in precipitation methods, our results are entirely consistent with published inorganic and microbially-mediated experimental siderite clumped isotope data, suggesting that siderite Δ_{47}-temperature dependence differs from Ca-Mg carbonates for reasons unrelated to precipitation methods. Our isotopic results are also consistent with published isotopic measurements on natural siderites precipitated at known environmental temperatures. Our analysis leads us to conclude that supersaturation-related kinetic effects likely play an important role in clumped isotope fractionation in natural and experimentally precipitated siderite.

Keywords: siderite, carbonate synthesis, clumped isotopes, stable isotopes

1. Introduction

Siderite ($FeCO_3$) is a geologically important ore mineral found in a diversity of settings worldwide. It forms in reduced environments, modern examples of which are organic carbon-rich Amazon shelf sediments (Zhu et al., 2002), low-sulfate ferruginous lakes (Wittkop et al., 2014) and hydrothermal veins (Žák et al., 2005). Siderite is common in Precambrian iron formations (IF; French, 1973; Klein, 1973; Floran and Papike, 1978; Konhauser et al., 2017), which chronicle the evolution of Earth's ocean from anoxic to oxygenated conditions, and it is thought that siderite played an important role in Fe and C cycling in the early ocean (Holland, 1984; Klein, 2005; Tosca et al., 2019). In the more recent geologic record, pedogenic siderite that formed from waterlogged soils are expected to record a multi-year average of mean annual air temperature (MAAT), making them an important target for reconstruction of ancient hydrologic cycles (White et al., 2001; Poulsen et al., 2007; Ludvigson et al., 2013; Fernandez et al., 2014). Beyond Earth, Fe-bearing carbonate minerals are a conspicuous component in the ALH84001 Martian meteorite (Harvey and McSween, 1996; Halevy et al., 2011) and have been identified at multiple locations on the Martian surface, including Gusev Crater, Gale Crater, and Jezero Crater (Morris et al., 2010; Horgan et al., 2020; Zastrow and Glotch, 2021, Tice et al., 2022), all of which have been visited by rovers. Future returned samples from Jezero Crater will almost certainly contain Fe-bearing carbonates, and these samples have the potential to provide insight into the climate and astrobiological history of Mars.

Because carbonate minerals preserve signatures of parent fluid chemistry through stable isotopes incorporated in their mineral lattice, their use as paleoclimatic records is well-established. Siderite oxygen isotope ratios ($\delta^{18}O$) have been used to develop a temperature-dependent carbonate-water isotope exchange equation that can be used to determine the

temperature of mineralization (Carothers et al., 1988; van Dijk et al., 2018). However, carbonate-water oxygen isotope paleothermometry requires that $\delta^{18}O$ of the parent fluid is either known or estimated, and this value is poorly known in most geologic applications (Henkes et al., 2018; Ryb and Eiler, 2018; Galili et al., 2019). A related but alternative isotope thermometer, carbonate clumped isotopes, is based on the thermodynamic preference of ^{13}C and ^{18}O to form bonds with each other rather than with lighter isotopes as temperature decreases; this is a useful alternative to traditional oxygen isotope thermometry because the formation of these heavy 'clumps' (in this case, ^{13}C-^{18}O) is independent of fluid $\delta^{18}O$ (Ghosh et al., 2006; Schauble et al., 2006). Thus, it is possible to determine a carbonate mineralization temperature from a single measurement. Carbonate clumped isotopes are reported as the value Δ_{47}, a relative measure of the abundance of the mass 47 isotopologue ($^{13}C^{18}O^{16}O$) of CO_2 evolved from phosphoric acid digestion of carbonate minerals (Ghosh et al., 2006; Eiler, 2007). Temperature calibration of the clumped isotope paleothermometer is well-established for calcium carbonates (Bonifacie et al., 2017; Petersen et al., 2019; Anderson et al., 2021), however, calibration of this isotope thermometer to siderite has not yet reached the same level of maturity (Fernandez et al., 2014; van Dijk et al., 2019).

Previous temperature calibrations of siderite Δ_{47} are equivocal about the effect of differing mineralogy or cation chemistry on carbonate Δ_{47}. Two recent composite calibrations (Bonifacie et al., 2017; Petersen et al., 2019) included siderite Δ_{47} data from experimental precipitates at 21, 39 and 51 °C (Fernandez et al., 2014), concluding that there was no obvious difference between Ca-, Mg-, or Fe-carbonates in that temperature range. However, van Dijk et al. (2019) showed that siderite precipitated between 8.5 and 62 °C follows the same relationship between Δ_{47} and temperature as reported by Bonifacie et al. (2017), but with a different y-

intercept. They hypothesized that the phosphoric acid digestion fractionation factor (AFF) for siderite clumped isotope measurements may differ from that of Ca-carbonates. However, several aspects of laboratory siderite synthesis by active degassing (Fernandez et al., 2014; van Dijk et al., 2019) could result in similar offsets, including ^{18}O enrichment of the parent fluid due to evaporation and kinetic isotope effects associated with CO_2 degassing (Affek and Zaarur, 2014).

All siderite Δ_{47} temperature calibration studies have synthesized carbonate from a fluid using an active degassing method, which both increases the pH of an Fe- and DIC-bearing fluid to the point that it achieves siderite saturation and ensures anoxic conditions during precipitation, which is crucial for preventing Fe-oxidation in siderite precipitation experiments (Kim and O'Neil, 1997; Wiesli et al., 2004; Fernandez et al., 2014; van Dijk et al., 2018). In this method, CO_2 is continuously bubbled in ultrapure water to form an anoxic, low-pH carbonic acid solution. This solution is slowly titrated on the benchtop with a concentrated Fe-solution, with the low pH of the DIC solution acting to prevent siderite nucleation. Once the desired Fe concentration is reached, CO_2 is sparged from solution by switching to an N_2 gas stream; this causes CO_2 to degas from solution, thus raising the pH and triggering siderite precipitation. Although CO_2 degassing decreases DIC in this method, alkalinity of the solution is conserved. In these experiments, temperature is controlled using a thermostatic water bath. Additionally, van Dijk et al. (2019) analyzed samples from van Dijk et al. (2018), who had effectively increased the equilibration rate of $\delta^{18}O$ between bicarbonate and water by adding the enzyme carbonic anhydrase (CA), which catalyzes the hydration of CO_2 and dehydration of HCO_3^- (Lindskog and Coleman, 1973; Watkins and Hunt, 2015). Van Dijk et al. (2018) also conducted several thermostatic, microbially-mediated precipitation experiments, which, because of the slow kinetics of abiotic siderite precipitation (Jimenez-Lopez & Romanek, 2004), allowed for biotic

siderite synthesis below 35 °C. In these experiments too, isotope disequilibrium was compensated for by the addition of CA to the microbial cultures.

Potential problems with the Fernandez et al. (2014) and van Dijk et al. (2018) siderite precipitations for clumped isotope temperature calibration are kinetic isotope effects (KIE) associated with CO_2 degassing (Kluge et al., 2013; Affek and Zaarur, 2014) or rapid nucleation and precipitation from a highly supersaturated solution. Regarding the former, there is a growing appreciation that nucleation of amorphous iron carbonate (AFC), the precursor phase for crystalline siderite, from solution requires a high degree of supersaturation (Dideriksen et al., 2015; Jiang and Tosca, 2019; Jiang & Tosca, 2020), which in turn necessitates a high concentration of dissolved inorganic carbon (and iron) in solution. The high DIC concentration required to attain this level of saturation results in fluid chemistry in which there is a strong tendency for CO_2 to degas into the headspace of a reaction vessel, particularly if that headspace does not contain CO_2. In the case of degassing experiments, like those of van Dijk (2018) and Fernandez (2014), efforts were taken to minimize or eliminate headspace, but the very nature of the experiment in which dissolved CO_2 is replaced with N_2 (g) has the potential to promote KIE associated with solution degassing coincident with carbonate precipitation (i.e., from a residual DIC pool containing kinetically fractionated DIC). For calcite, Levitt et al. (2018) investigated the effect of precipitation rate and temperature on Δ_{47} through seeded growth chemostatic experiments and found that there was an inverse relationship between Δ_{47} and supersaturation at low temperature (0-25 °C). These results imply that calcite precipitated at high supersaturation is likely to be the furthest from clumped isotope equilibrium. If the findings of Levitt et al. (2018) for calcite apply to siderite, saturation state may influence fractionation for both Δ_{47} and $\delta^{18}O$. In addition to the effects on $\delta^{18}O_{DIC}$ disequilibrium from degassing, there is some indication that

AFC nucleation and siderite crystallization may result in KIE for carbon isotope values due to rapid precipitation once the threshold for precipitation is reached (Jiang and Tosca, 2019; Jiang et al., 2022).

An explicit test of the active degassing method for laboratory siderite precipitation is experimental siderite precipitations under conditions that: (1) do not rely on degassing as a means of raising solution pH to initiate siderite precipitation, (2) minimize the volume of headspace available for degassing of a DIC-rich solution, and (3) maintain static fluid chemical conditions ("constant composition") as a means of controlling the siderite precipitation rate. In the constant composition method (Zhong and Mucci, 1989; Mucci and Morse, 1983; Tang et al., 2003; Beck et al., 2013), precipitation rate is controlled through addition of titrants to a bicarbonate "working solution" to maintain a constant pH, ionic strength, and supersaturation. This method has been shown to be effective for controlling precipitation rates in several mineral phases, including calcite (Kazmierczak et al., 1982; Levitt et al., 2018), aragonite (Westin and Rasmuson, 2005), vaterite (Spanos and Koutsoukos, 1998), and calcium phosphate (Koutsoukos et al., 1980). To our knowledge, constant composition experiments have not been previously used to precipitate siderite.

Here, we present the results from a modified version of the Beck et al. (2013) constant composition technique for siderite precipitation and use the experimental precipitates to evaluate equilibrium oxygen and clumped isotope fractionation as a function of solution temperature. Our experimental methods allow us to evaluate the effects of degassing and supersaturation on the stable isotope ratios of synthetic siderite and verifies the importance of the solution Fe^{2+} to DIC ratio (Fe:DIC) in determining the Fe-carbonate phase that precipitates (Jiang and Tosca, 2019; Koo and Kim, 2020). In principle, our method allowed for precise pH control (±0.1 pH units),

which maintains a constant precipitation rate as titrants are added. We discuss the advantages and challenges of this method for inorganic siderite precipitation, and how those relate to equilibrium oxygen isotope exchange between water and siderite and siderite clumped isotope temperature dependence. We evaluate our experimental and isotope data relative to published oxygen and clumped isotope temperature relationships for siderite (Fernandez et al., 2014; van Dijk et al., 2019) and discuss the process of homogeneous nucleation of siderite from a fluid and the implications for equilibrium isotope fractionation in natural Fe-carbonate-saturated solutions.

2. Methods

2. 1.1. Constant Composition Siderite Precipitation Experiments

All experiments were conducted in a Coy polymer anoxic glovebox, which was purged every 12 hours with a gas mix of 95% N_2/5% H_2. The purpose of the H_2 was to react with any residual oxygen using a palladium (Pd) catalyst to form H_2O, which was subsequently removed using a $CaSO_4$ desiccant; this maintained anoxic conditions for experimental timescales. The catalyst and desiccant were rejuvenated weekly by drying in a 150 ºC oven for at least 2 hours to maintain optimum functionality. O_2 and H_2 levels were constantly monitored using a Coy CAM-12 gas analyzer, which has an effective detection limit of 20 ppm O_2, to verify that O_2 was at or below detection limit for the duration of the experiments.

In our constant composition siderite precipitation experiments, three solutions were prepared: (1) a working solution in the main reaction vessel, (2) a lower pH titrant solution containing the dissolved iron (Fe) needed to replace Fe lost to siderite precipitation, and (3) a second, higher pH titrant containing the dissolved inorganic carbon (DIC) needed to replace DIC lost to precipitation and counteract any pH changes caused by $FeCl_2$ addition and siderite precipitation. All solutions were prepared with ultrapure (18.2 mΩ) deionized (DI) water that was deoxygenated via bubbling with O_2-free ultrapure N_2 for two hours, then transferred to the glovebox and allowed to stir in the glovebox atmosphere for an additional 24 hours. This allowed any residual oxygen to escape from solution and be removed by the Pd catalyst. Working solutions were designed to set the experimental DIC concentration, pH, and ionic strength using $NaHCO_3$, HCl/NaOH, and NaCl, respectively. Iron stock solutions (1 molal) were prepared with Fe(II)-chloride powder (Beantown Chemicals); the resulting solution was then acidified to a pH of 1-2 using HCl and allowed to chemically reduce for 48h to ensure no Fe^{3+} was present, using

methods similar those described in Jiang & Tosca (2019). Prior to use in a precipitation experiment, the stock solution was diluted to 0.1 molal to prevent instantaneous nucleation upon injection to the working solution. The DIC titrant was prepared using $NaHCO_3$, Na_2CO_3, and NaCl. Desired titrant concentrations (Table S1) were determined using a MATLAB script that calculates the DIC concentrations needed to maintain pH given the concentrations of the working solution, starting pH, and temperature.

Precipitations were conducted in a 500 mL multi-port glass jacketed reaction vessel (Fig. 1) connected to a heated water circulator to maintain constant temperature within the vessel. For 15 °C experiments, a cold finger was placed inside the water circulator as a cooling thermostat. The vessel and 4-port lid were placed in the glovebox for a minimum of 4 hours before each experiment began to ensure that the vessel did not contribute O_2 to the glovebox atmosphere. The reaction vessel was connected to a Metrohm 902 Titrando equipped with two 800 Dosino units for DIC and dissolved Fe titrant delivery through the vessel ports. The autotitrator was also connected to a Metrohm pH and temperature electrode, housed in the third vessel port, to monitor solution conditions for the duration of an experiment. Titration was controlled by the Tiamo software package, which can be programmed to perform many types of titrations and, in this case, was used to set pH endpoints for addition of acidic Fe titrant and alkaline DIC titrant. The fourth vessel port was used for manual solution sampling with a syringe but remained sealed in-between sampling to avoid solution degassing effects during active precipitation.

Before beginning an experiment, the working solution was transferred to the reaction vessel and the vessel lid was placed onto the reaction vessel. The contact point between the vessel and the lid was wrapped with Parafilm and Teflon tape and locked in place with a C-clamp. The four ports in the vessel lid, containing the titrant lines, pH electrode, and blank

sampling port were also wrapped with Parafilm and Teflon tape. The working solution was then allowed to stir at the experimental temperature for a minimum of 24 h before beginning an experiment to ensure oxygen isotope equilibrium between DIC and H_2O (Beck et al., 2013; Uchikawa et al., 2021) and was stirred constantly for the experimental duration. In five of our experiments (75-2B, 15-2A, 25-3A, 50-4C, 15-1C), the vessel-lid contact was also sealed with silicone vacuum grease to further mitigate against evaporation and/or degassing of the solution into the glovebox atmosphere. After the equilibration period, the experiments were initiated by a series of manually controlled injections of $FeCl_2$ titrant (0.1 molal) from one of the Dosino units to set the $[Fe^{2+}]$ at a desired concentration of either 0.001 or 0.0025 molal. The same $FeCl_2$ titrant was used for further titration from the Dosino unit by the Tiamo autotitrator control software after the initial injections were completed and the constant composition experiment was begun. Target concentrations were designed to achieve a level of saturation defined by the relationship:

$$(1)\ SI = log\ (IAP)_{AFC} - log\ (K_{crit})$$

where IAP_{AFC} is the ion activity product defined for AFC, by Jiang & Tosca (2019) as:

$$(2)\ IAP_{AFC} = \frac{a_{Fe^{2+}} \times a_{CO_3^{2-}}^{0.5}}{a_{H^+}}$$

AFC was demonstrated by those authors to be the precursor to the crystalline Fe-carbonate minerals chukanovite and siderite. K_{crit} is the critical supersaturation at which AFC begins to nucleate, defined in Jiang & Tosca (2019) as $\log(IAP_{AFC}) = 2.20$ at 25°C. We recalculated this value in terms of HCO_3^- using the methods described in Singer and Stumm (1970) and extrapolated across the relevant temperature range using a Van't Hoff expression. Thus, our definition of SI describes the targeted initial concentration of solution components relative to an experimentally determined log K for AFC nucleation and ranged from SI = 0.74 to 2.11 at the

time that precipitation was observed to initiate. It is important to note that K_{crit} is not strictly a solubility product (K_{sp}) due to the lack of thermodynamic data for AFC; however, we assert that this experimentally derived value is sufficient for our calculations because our goal was to achieve a sufficiently high supersaturation for homogeneous nucleation of AFC from the working solution (Dideriksen et al., 2015; Jiang and Tosca, 2019). Initial Fe injections were completed at a rate of 1 mL/hour, with 0.5 mL injected every 30 minutes using the autotitration system. Once the iron injection was complete, the titration was initiated. Working solution pH before initial injections ranged from 7.9-8.8; set pH for titrations ranged from 7.9-8.5. Each experiment was allowed to run for 2-6 days, at which time they were terminated and precipitates were prepared for analysis. A summary of all targeted and observed experiment conditions is provided in Table 1.

At experiment termination, precipitates were vacuum filtered from the working solution (0.45µm nitrocellulose filters), placed in a glass vacuum-sealed container, and dried immediately on a vacuum line for approximately 8 hours. Dried precipitates were then analyzed on a Rigaku Miniflex powder X-ray diffractometer (XRD) to verify mineralogy and assess crystallinity. To minimize oxidation, samples were packed on a zero-background flush and magnetically sealed inside a Rigaku air-sensitive domed sample holder. The dome was removed immediately before analyses began due to the high background of the dome material; total air exposure time was <30min. XRD scans were conducted from 15-70 2θ at a step size of 0.02°, with a collection time of 10°/min.

2.1.2. Titrant Calculation

The theory behind calculation of the titrant concentrations is described in detail by Beck et al. (2013). Briefly, the script mentioned in Section 2.1.1. calculates the initial carbonate

system equilibrium of the working solution at 15, 25, 50, or 75ºC, and calculates ion activity coefficients using the B-dot expansion of the Debye-Hückel equation, which adds a deviation factor Ḃ to account for divergence from predicted ion activity coefficients (H.C. Helgeson, 1969; H.C. Helgeson, 1969; Helgeson and Kirkham, 1974; Lewis et al., 2020). The script then recalculates equilibrium of the carbonate system of the working solution in response to an arbitrary increment of siderite precipitation. Titrant concentrations are calculated based on restoring the working solution to the initial carbonate system equilibrium state and uses dissociation constants and relationships for interdependencies of the equilibrium carbonate system from Zeebe and Wolf-Gladrow (2001).

2.2. Siderite Heating Experiments

In order to measure the acid fractionation factor associated with siderite dissolution during phosphoric acid digestion and CO_2 collection, a siderite sample with an equilibrium clumped isotope value achieved by high-temperature, solid-state re-equilibration of carbonate isotopologues (Passey and Henkes, 2012) was required. We prepared such a sample by heating a siderite powder derived from single crystal hydrothermal siderite (JMP-Sd-1, a hydrothermal siderite from the Julcani Mine region, Peru) in a high temperature piston-cylinder apparatus. A mixture of coarse (60-120 μm) and fine (<60 μm) siderite grains were packed into a silver capsule with a tight-fitting lid. Two different size fractions were selected to enable the capsule to be packed as completely as possible, with fine material filling the pore space between larger grains, while also avoiding potential complications that might be caused by packing the capsule entirely with the finest material, which might be more subject to oxidation owing to its higher surface area. The packed capsule was dried in a vacuum oven at 120 °C for 6 hours. The rest of the experimental assembly consisted of an outer talc cell wrapped in lead foil, a graphite furnace,

pyrophyllite spacers above and below the sample, and an insulating ceramic sleeve keeping the capsule out of direct contact with the furnace. The dry, assembled cell was immediately loaded into the ¾" piston-cylinder apparatus to prevent re-adsorption of water.

Experimental conditions were selected for maximum heating without risk of siderite decomposition (Kang et al., 2015). The sample was initially pressurized to 1.2 GPa at room temperature before heating to 625 °C. Once at the target temperature, the pressure was reduced to 1.0 Gpa. The sample was held at these P-T conditions for 72 hours, then subjected to a rapid isobaric quench using water circulated through the piston cylinder apparatus, which reached room temperature in <20 seconds. The capsule was then recovered and dry-sawed open and the sample powder retrieved. The sample was immediately characterized by XRD using the method described in Section 2.1.

2.3. Stable Isotope Analysis

Carbon, oxygen, and clumped isotope measurements were conducted in the Department of Geosciences at Stony Brook University on a Thermo Scientific MAT 253 Plus isotope ratio mass spectrometer coupled to a custom-built, automated acid digestion and sample purification system similar to the one described in Henkes et al. (2013). ~7 mg aliquots of siderite were reacted at 90 ºC for 60 minutes in the online, common phosphoric acid bath to ensure complete digestion. The extended time of digestion is necessary for siderite as the dissolution kinetics of siderite are very slow relative to calcite (Rosenbaum and Sheppard, 1986). Reactions were considered complete when small bubbles were no longer observed in the acid bath and pressure measurements in the closed acid reaction volume had returned to baseline values. Every analysis included in this study achieved these conditions in <60 minutes of acid digestion. As a test of these digestion conditions, and as an internal standard, we also measured aliquots of a late

Carboniferous (Pennsylvanian) siderite nodule from the Mazon Creek fossil beds in the Francis Creek Shale Member (sample 'MC-Full', Grundy County, Illinois, USA). This sample yielded an average (n = 8) $\delta^{13}C$ = 3.55 ± 0.40‰ (± 1 SD, VPDB), $\delta^{18}O$ = -1.24 ± 0.25‰ (± 1 SD, VPDB), and Δ_{47} = 0.543 ± 0.019‰ (± 1 SE, $CDES_{90}$), which are consistent with Controneo et al. (2016) and the shallow burial conditions of nodule cementation, indicating that our methods achieve sufficient digestion of natural siderite samples.

Accurate reporting of carbonate clumped isotopes requires establishing a reference frame that accounts for fragmentation and recombination in the mass spectrometer ion source and other analytical artifacts (Huntington et al., 2009; Dennis et al., 2011). This allows clumped isotope measurements to be reported on a common scale across all laboratories, the so-called 'carbon dioxide equilibrium scale' (Dennis et al., 2011). To construct this reference frame, we regularly analyzed purified CO_2 that was either heated to isotopic equilibrium at 1000 °C or equilibrated with water at 30 °C (Table S2). The former was prepared by heating CO_2 aliquots sealed in quartz tubes in a tube furnace at 1000 ºC. The latter was aliquoted from two thermostatic tanks containing ~15 psi CO_2 and <5 mL of water with varying $\delta^{18}O$ attached to the carbonate device used to generate sample data. One of these reference gases was analyzed every 1-2 days, thus ensuring that all four gases were measured on a weekly to sub-weekly basis. These gases were introduced in a He carrier gas in the second stage in the purification sequence and were thus treated in the exact same manner as carbonate samples minus the acid digestion.

All samples, carbonate standards, and reference gases were analyzed at a dual inlet bellows pressure corresponding to a signal of either 12 or 16 V on the Faraday cup measuring mass 44 CO_2. The dual inlet measurement sequence consisted of seven repetitions of ten cycles for a total integration time of 1400s. All CO_2 was measured against a pure reference gas (Oztech

Trading Corporation, Safford, AZ) with $\delta^{13}C$ = -3.59‰ VPDB and $\delta^{18}O$ = 24.91‰ VSMOW. The long-term average standard error of Δ_{47} for the seven repetitions of ten cycles was <0.010‰. Δ_{47} values were calculated using the IUPAC ^{13}R, ^{17}R, and ^{18}R from Brand et al. (2010) and as recommended by Petersen et al. (2019) for Δ_{47}-temperature calibration studies. The siderite precipitates were run in triplicate when possible (some precipitates oxidized while aliquots were being weighed and could not be run again) and we report average $\delta^{13}C$, $\delta^{18}O$, and Δ_{47} values in Table 2. All Δ_{47} values are reported as measured, with an implied 90°C fractionation, and thus reported as "$CDES_{90}$" (Bonifacie et al., 2017).

The international calcium carbonate standards IAEA-603 and NBS-18 were used to correct measured $\delta^{13}C$ and $\delta^{18}O$ values, sometimes with a two end-member linear regression correction scheme when both standards were run in the same analytical session (Table S2). Working or 'internal' carbonate standards included SBU-Carrara, a marble similar to IAEA-603, with an average Δ_{47} = 0.295 ± 0.024‰ (n = 17, ± 1 SD, $CDES_{90}$), HC-1, chicken eggshell from East Setauket, NY, USA, with Δ_{47} = 0.525 ± 0.014‰ (n = 11, ± 1 SD, $CDES_{90}$), and two interlaboratory calibration standards, ETH-2 and ETH-4, with Δ_{47} = 0.206 ± 0.017‰ (n = 13, ± 1 SD, $CDES_{90}$) and Δ_{47} = 0.447 ± 0.019‰ (n = 8, ± 1 SD, $CDES_{90}$), respectively. The interlaboratory calibration standard values are indistinguishable from the accepted values for both calcium carbonates (Bernasconi et al., 2021), and our value for SBU-Carrara is indistinguishable from the consensus value for IAEA-C1, a Carrara marble ^{14}C activity standard (Bernasconi et al., 2021).

Before the initial $FeCl_2$ injections and at experiment termination, 1.5 mL aliquots of solutions were sampled and subsequently analyzed for $\delta^{18}O$ in the Organic and Stable Isotope Biogeochemistry Lab at the University of Buffalo on a Picarro 2130i cavity ringdown laser

spectrometer. Measured values were corrected for instrument memory and drift and normalized to VSMOW according to Picarro protocols (van Geldern & Barth 2012) using in-house standards and quality control samples.

3. Results

3.1 Solution Conditions During Experiments

Here, we first present results for precipitates derived from what we consider well-controlled, chemo-static experiments, that is, those in which pH was maintained within a range of ±0.1 pH units of the target pH for the experiment and required no manual intervention to correct for problems with the titration program (described below). We then discuss experiments considered to be less well-controlled; the potential consequences for isotope results from precipitates of less well-controlled experiments is discussed in Section 4.4.

There are four experiments that we consider well-controlled and chemostatic, with only very small pH fluctuations over the course of experimentation. These are 15-1A and 15-2A at 15 °C, 25-3A at 25 °C, and 50-4C at 50 °C. Experiments at 75 °C, discussed in more detail in the following paragraph, displayed larger pH fluctuations and are thus considered less well-controlled. Figure 2 shows the measured pH and modeled solution conditions during 25-3A as a representative example of a chemo-static experiment. The model, applied after experiment completion, uses the measured pH and volumes of added titrant recorded by the Tiamo software to calculate all solution conditions assuming that, for each added aliquot of Fe-titrant, 25, 33, 50, 66, or 75% of the added Fe^{2+} precipitated as siderite. The model results illustrate that, when pH remains constant, all parameters increase throughout the course of the experiment, assuming that precipitation rate also remains constant. For these experiments, [Fe^{2+}] rises from initial concentrations (at the beginning of titration) of either 0.001 or 0.0025 mol/kg to modeled final concentrations of 0.0035 — 0.04 mol/kg. Initial DIC concentrations range from 0.015-0.3 mol/kg, and modeled final concentrations range from 0.01 to 0.6 mol/kg. Fe:DIC ratios increase even during the most well-controlled experiments, indicating that the titration required the

addition of more of the $FeCl_2$ stock solution in order to maintain constant pH. Ionic strength shows the sharpest increase of the calculated parameters (0.415-0.46 to 0.545-1.65) due to the addition of Na^+ and Cl^- from both titrants. Saturation (SI) increased during the initial Fe^{2+} injection phase, then leveled out at the onset of nucleation. In well-controlled experiments, nucleation occurred when SI is between 0.74-2.11.

In the less well-controlled experiments between 15-50°C, we observed that after the initial $FeCl_2$ injection pH fluctuations were more dramatic, often exceeding 0.1 pH units, but not greater than 1 pH unit. In some cases, the titration program was unable to determine which titrant to add in response to these rapid pH fluctuations. This led to what we term a 'runaway titrant addition,' in which the program continued adding titrant past the set pH; the program then needed to be stopped and restarted to restore pH control. Figure 3 shows the measured pH and modeled solution conditions of experiment 25-1B, in which pH appears to be very stable, but has 4 large excursions corresponding to excessive titrant addition and subsequent recovery. Increases in both [Fe^{2+}] and [DIC] have a stepped pattern, in contrast to the near-constant rate of increase shown in Figure 2.

In two of the three experiments conducted at 75 °C, excessive evaporative loss of the working solution was caused by an incompletely sealed reaction vessel. In the third experiment, no evaporation was observed, which we attribute to the addition of silicone vacuum grease to the vessel-lid seal. While pH fluctuations exceeded 0.1 pH units in this experiment, the titration program did not need to be stopped at any point during the experiment. Solution conditions in this experiment (75-2B) are shown in Figure 4. The pH setpoint for this experiment was 8.2. Despite this, almost immediately after the start of the titration program, the auto-titrator added DIC in a runaway titrant addition. In response, the titrator added [Fe^{2+}] approximately a

third of the way into the experiment, resulting in an increase in [Fe^{2+}] (modeled from 0.001-0.002 to 0.012-0.034) and corresponding with a decrease in pH and a sharp increase in Fe:DIC. The pH stabilized at 8.2 for a period of time before another uncontrolled excursion to pH 8.5 occurred. At this point, the experiment was terminated.

3.2 Solid Phase Preparation and Characterization

XRD analyses show that siderite was successfully produced at all temperatures (Fig. 5 and summarized in Table 1). In all reported experiments and sample processing, the secondary formation of oxidation products of the siderite (e.g., ferrihydrite) was not present in XRD patterns collected on the samples. Samples with detectable oxidation (indicated by both color change and oxide peaks in the XRD scan) were discarded, not used for isotope analysis, and are not discussed further.

In three samples (15-1C, 25-1A, and 50-4C), a mixture of siderite and chukanovite ($FeCO_3(OH)_2$) was precipitated. Chukanovite is easily identified in an XRD pattern by its characteristic doublet peak at 34 and 35º 2θ (Cu-Kα; Fig. 6). Other recent synthesis experiments suggest that chukanovite formation is highly dependent on the Fe:DIC ratio in the working solution (Jiang and Tosca, 2019; Koo and Kim, 2020). The majority of the experiments we report on here were designed to target an initial Fe:DIC 0.003-0.01 for the experimental duration, which resulted in the precipitation of siderite alone. In the three experiments where chukanovite was identified, however, we purposely targeted a lower supersaturation to assess whether there are observable differences in isotope ratios between different fluid supersaturation at the same temperature. This lower supersaturation necessitated a higher Fe:DIC ratio (0.05-0.07), which resulted in precipitation of a siderite-chukanovite mixture. To illustrate these effects, Figure 7 shows Fe speciation and saturation with respect to siderite as a function of the activity of HCO_3^-

and temperature. This diagram was constructed using the "TACT" temperature-activity plotter in Geochemist's Workbench with typical conditions from our experiments as inputs (Table 1): Fe^{2+} = 0.001M, Na^{+} = 0.35M, Cl^{-} = 0.1M and a pH = 8.35. TACT calculates activity coefficients based on the input concentrations (and ionic strengths calculated from them) using the B-dot expansion of the Debye-Hückel equation. TACT solves for siderite saturation as a function of temperature by calculating a polynomial fit to the $\log K_{sp}$ values contained in the Geochemist's Workbench thermo.dat database for siderite. The temperature dependent K_{sp} values for siderite in this database were calculated using methods described in Johnson et al. (1992), which relies on reference state data (298.15 K, 1 bar) for siderite in Helgeson (1978). We also show conditions of our experimental solutions superimposed on this stability field, using the targeted experiment values (Table 1) as input into a Geochemist's Workbench GSS spreadsheet, which then calculates the speciation of these solutions so that they can be plotted in T-activity space. To initiate precipitation, our solutions required significant supersaturation relative to the expected condition for siderite saturation at all temperatures, in accord with previous studies (Dideriksen et al., 2015; Jiang and Tosca, 2019; Jiang and Tosca, 2020). Our experimental data also delineate an apparent temperature-invariant Fe^{2+}/HCO_3^- boundary ($\log Fe^{2+}/HCO_3^- = -2$ for Fe^{2+} = 0.001M) that subdivides experiments that precipitate only siderite (at $\log Fe^{2+}/HCO_3^- < -2$ and higher supersaturation level relative to siderite) and those that precipitate a mixture of chukanovite and siderite (at $\log Fe^{2+}/HCO_3^- > -2$ and lower supersaturation level relative to siderite).

3.3 Stable Isotope Analysis

The results of carbon ($\delta^{13}C$), oxygen ($\delta^{18}O$), and clumped isotope (Δ_{47}) analyses are shown for all experiments in Table 2. Carbon isotope values ($\delta^{13}C$) of the siderite precipitates

(chukanovite-bearing precipitates excluded) range from -6.90 to -5.91‰ (VPDB), with a mean of -6.55 ± 0.14 (1σ SD), and do not vary as a function of temperature. This is expected because all solutions were prepared with the same carbon sources (*i.e.*, $NaHCO_3$ in the working solution and titrant solution and Na_2CO_3 in the titrant solution). The carbon sources have $\delta^{13}C$ values of -7.19 ($NaHCO_3$) and -7.92‰ (Na_2CO_3) VPDB, with $NaHCO_3$ comprising the larger of the two carbon sources by mass added (~10:1) to solution. Figure 8 shows measured carbon isotope ratios, recast as $\varepsilon_{FeCO3\text{-}HCO3}$ values, as a function of temperature. $E_{FeCO3\text{-}HCO3}$ is given by:

$$(3)\ {}^{13}\varepsilon_{FeCO_3-HCO_3^-} = ({}^{13}\alpha_{FeCO_3-HCO_3^-} - 1) \times 10^3$$

Where α is:

$$(4)\ {}^{13}\alpha = \frac{1000 + \delta^{13}C_{FeCO_3}}{1000 + \delta^{13}C_{HCO_3^-}}$$

It is justified to approximate the $\delta^{13}C$ value of the DIC source as that of the bicarbonate ion, as $NaHCO_3$ is the dominant carbon source. There is a ^{13}C enrichment of the order of 1‰ in the precipitated carbonate relative to the DIC (Fig. 8). At pH ~8.5, DIC is dominated by HCO_3^- (pK_A for HCO_3-CO_3 ≅ 10.5 between 15-75 °C) and this small enrichment is expected from the difference in vibrational frequencies between the bicarbonate ion and carbonate minerals and is consistent with the calcite precipitation experiments of Romanek et al. (1992; Fig. 8). Recent data from Jiang et al. (2022) is also included. Interestingly, there is a difference in carbon isotopes between pure siderite samples and chukanovite-bearing samples, with chukanovite-bearing samples yielding lower $\varepsilon_{FeCO3\text{-}HCO3}$ relative to siderite precipitated at the same temperature. Finally, there do not appear to be any systematic differences in $\varepsilon_{FeCO3\text{-}HCO3}$ between

experiments with silicone vacuum grease applied to the reactor vessel-lid seal ("sealed experiments," Fig. 8) and those that did not ("unsealed experiments" in Fig. 8).

The oxygen isotope values of the precipitation fluids ($\delta^{18}O$) are shown in Table 3. Tap water for Suffolk County, NY, from which our DI water was sourced, typically has a $\delta^{18}O$ value of -7.4‰ (VSMOW). For some experiments, initial fluid aliquots were not available, in which case we assumed that the initial $\delta^{18}O$ value was equal to the tap water value. The fluid $\delta^{18}O$ results indicate changes in the $\delta^{18}O$ value of water that range from -0.01‰ to -1.02‰, with the "unsealed" experiments in which no silicone vacuum grease was applied to the vessel lid exhibiting somewhat larger differences between initial and final values. Notably, the initial water sample from experiment 75-1A is distinctly ^{18}O-rich, indicating that substantial evaporation had occurred before initiation of the precipitation experiment and that evaporative loss continued during experiment, resulting in a final $\delta^{18}O$ = -3.83‰. This result is consistent with observed condensation on the inside of the glovebox walls during this experiment and obvious visible water loss from the reaction vessel, likely caused by the absence of a silicone vacuum grease seal. Experiment 75-2B had a silicone vacuum grease seal, there was no observable water loss from the vessel, and the oxygen isotopic composition of waters from this experiment are consistent with area tap water $\delta^{18}O$.

Figure 9 shows temperature ($10^3/T(K)$) versus $1000\ln{}^{18}\alpha$ and shows our data compared to all published experimental siderite data (Carothers et al., 1988; Zhang et al., 2001; Fernandez et al., 2014; van Dijk et al., 2018). $^{18}\alpha$ is calculated analogously to Equation 4, substituting $\delta^{18}O_{FeCO3}$ and $\delta^{18}O_w$ for $\delta^{13}C_{FeCO3}$ and $\delta^{13}C_{HCO3-}$, respectively. In Figure 9, we omitted experiment 75-1A, which was compromised by evaporative water loss. Our chukanovite-bearing sample data are offset to low $1000\ln{}^{18}\alpha$ relative to pure siderite precipitates

at the same temperature and are also lower than published $1000\ln^{18}\alpha$ values at similar temperatures; thus, the chukanovite-bearing samples are also excluded from Figure 9. Our siderite $1000\ln^{18}\alpha$ data, however, are generally intermediate between legacy (Carothers et al., 1988) and more contemporary (Zhang et al., 2001; Fernandez et al., 2014; van Dijk et al., 2018) datasets in the same range of precipitation temperatures.

A plot of siderite Δ_{47} ($CDES_{90}$) versus $1000\ln^{18}\alpha$ is a useful way to evaluate precipitation with respect to both oxygen and clumped isotope equilibrium across our range of experimental temperatures (Fig. 10). All existing siderite clumped isotope data was recalculated to a 90°C reference frame to facilitate comparison with our experimental data. Of the precipitates measured, three differ markedly from the existing siderite clumped isotope data (Fig. 10A; Fernandez et al., 2014; van Dijk et al., 2019): 50-4C; 25-1A; and15-1C, yielding low $1000\ln^{18}\alpha$ and high Δ_{47} relative to other samples precipitated at the same temperature. These samples are marked with a 'C'. As discussed in Section 2, these three experiments were conducted with a higher initial Fe:DIC than the other precipitation experiments and chukanovite was detected in the XRD patterns of all three precipitates. On average, the precipitates containing only siderite plot with published siderite clumped isotope data and lie along a line defined by the predicted relationship between Δ_{47} and $1000\ln^{18}\alpha$ as a function of temperature from the experimental precipitates of van Dijk et al. (2018) and (2019). One exception to this is experiment 50-3A, which plots noticeably above the majority of siderite clumped isotope data despite its pure siderite mineralogy. Siderite Δ_{47} for all published precipitates (including our own) is still negatively offset by ~0.05‰ from the predictions of published composite clumped isotope calibrations (Bonifacie et al., 2017; Petersen et al., 2019).

The data from this study can be further subdivided based on the experimental parameters that were realized during precipitation in an effort to ascertain whether $\delta^{18}O$ and Δ_{47} of our precipitates were affected by factors such as: (1) the quality of the vessel-lid seal, which may have caused degassing or evaporation, (2) having full chemostatic control of the experiment (defined as having pH fluctuations ≤ 0.1pH units), and (3) the degree of saturation, and related differences in Fe:DIC ratio. Figure 10B shows siderite Δ_{47} versus $1000\ln^{18}\alpha$ and distinguishes between "sealed" (i.e., those in which silicone grease was applied to the vessel-lid contact) and "unsealed" (those sealed with only Parafilm and Teflon tape) experiments at all precipitation temperatures, as well as those experiments in which full chemostatic control was maintained over the course of experimentation. Finally, experiments conducted at lower saturation index and higher Fe:DIC (Fig. 7; ranging from 0.74-1.75 and 0.05-0.07) that produced a mix of chukanovite and siderite are marked with a "c". It is apparent from this parsing of the data that a grease-sealed vessel-lid contact does not obviously impact the isotope ratio of the precipitates, with the exception of experiment 75-1A that was significantly compromised by evaporation as a result of incomplete sealing of the reaction vessel. Full chemostatic control of the experiment also does not seem to affect the precipitate isotope values. Siderites from sealed and unsealed as well as chemostatic and non-chemostatic experiments all appear to scatter about the Δ_{47} versus $1000\ln^{18}\alpha$ relationship of van Dijk et al. (2018) and (2019), with no obvious systematic offsets linked to these experimental factors. The only outliers in the group are those experiments that were conducted under conditions appropriate to the formation of a mixed chukanovite-siderite precipitate.

Finally, the heated siderite sample described in Section 2.2 was confirmed by XRD to be siderite after 72 hours at 625°C, despite a slight darkening of the sample. The sample was

analyzed as described in Section 2.4, and the averages of three analyses are reported in Table 2. Carbon and oxygen isotope ratios of the heated sample (Jm-Sd-1-625) were within ±-1‰ and ±0.4‰, respectively, of the starting material (Jm-Sd-1) values. Because the oxygen isotope ratio of the heated sample is within measurement error of the unheated sample, the ~1‰ change in $\delta^{13}C$ after heating cannot be due to CO_2 degassing because that would require siderite decomposition to magnetite, which was not observed in the heated sample XRD spectra (Figure S1). We cannot rule out isotope exchange during heating with some unidentified carbon source with a lower $\delta^{13}C$ value (e.g., lathe oil used in the construction of the silver reaction capsule), though this is difficult to envision because the C mass balance in the closed reactor would be overwhelmingly in the direction of siderite.. Despite this, the Δ_{47} value decreased by 0.15‰, which is consistent with solid state ^{13}C-^{18}O bond reordering at an experimental temperature much greater than the native hydrothermal origin of this sample.

4. Discussion

4.1.1 Siderite Precipitation During Constant Composition Experiments

Attainment of chemostasis and mineral-water isotope equilibrium during carbonate precipitation requires finely tuned experimental conditions. For the carbonate system, Beck et al. (2013) demonstrate constant composition conditions and conclude that, even if pH remains constant, supersaturation of the solution may change due to other chemical factors, such as changes in ionic strength and exchange of CO_2 between the working solution and the atmosphere of the overlying headspace. The latter process is a particular challenge for anoxic experiments, required for siderite precipitation, as the working solution is typically in contact with a CO_2-free, N_2/H_2 glovebox atmosphere. Levitt et al. (2018) used the constant composition method to study $\delta^{13}C$, $\delta^{18}O$, and Δ_{47} fractionation in calcite. In this work, chemostatic seeded growth experiments were performed at 10, 20, and 30 °C for 70-240 hours and solution pH and temperature were maintained for the experimental duration. Oxygen isotope equilibrium was ensured at the experiment outset by allowing the DIC reagent to exchange with the working solution for a period of 4-10 days, and calcite supersaturation was low throughout the experiments to minimize isotope effects associated with rapid nucleation. Despite these efforts, their results demonstrated that rapid growth rate makes isotope equilibrium difficult to maintain, even at low calcite saturation states with seed crystals to reduce the nucleation barrier. For siderite, Jiang & Tosca (2020) used seeded growth experiments to study the growth rates and mechanisms of siderite growth from solution as a function of saturation state. These experiments did not use the constant composition method, as they used $[Fe^{2+}]$ consumption to calculate precipitation rate and the solution pH was controlled by a pH buffer. Nevertheless, they found that the rate of $[Fe^{2+}]$ consumption is faster as supersaturation increases. This implies that the high supersaturation

necessary for homogeneous siderite nucleation facilitates a faster growth rate. If the findings of Levitt et al. (2018) regarding $\delta^{18}O$ fractionation associated with calcite growth rate are true for siderite, and Jiang & Tosca (2020)'s connection between rapid siderite growth and increasing supersaturation is valid for constant composition experiments, then our siderite precipitation from supersaturated solutions may yield carbonate-water isotope disequilibrium even if chemostasis is maintained throughout the experiment.

As described in Section 3.1 and shown in Figures 2-4, the question of whether our experiments can be considered truly chemostatic is complex. In the experiments that were well-controlled with respect to pH, fluctuation in working solution pH was frequent but low in magnitude (±0.01 pH units). Our modeled solution conditions, which are based on titrant addition rates, indicate that [Fe], [DIC], ionic strength, and Fe:DIC increased throughout the experimental duration, with the magnitude of increase dependent on assumptions made about how much of the added titrant was precipitated as siderite. But even in the case of a low modeled precipitation efficiency (25% of added Fe and DIC precipitating as siderite), the increases in solution parameters are relatively small and were never greater than an order of magnitude for any chemical conditions during the experiments (25-3A; Fig. 2). Thus, we consider these to be effectively pH-static experiments and can therefore reasonably consider them to be chemostatic. In contrast, pH excursions in our less well-controlled experiments resulted in larger increases in one or more chemical parameters; for example, in 25-1B, a pH excursion of 0.985 pH unit led to an increase of Fe:DIC from ~0.05 to 0.1 (Fig. 3). Though the magnitude of total Fe:DIC change is similar between chemostatic and non-chemostatic experiments, as shown in Figures 2-4, the rate of change in experiments where pH excursions occurred is significantly greater (Fig. 11); thus, these experiments may be considered transiently chemostatic.

Despite the difficulty of achieving a truly chemostatic experiment, there are several advantages of this method for establishing conditions amenable to siderite stable isotope equilibrium. First, relative to the active degassing method (i.e., Fernandez et al., 2014; van Dijk et al., 2018), the closed-system design of constant composition experiments is less likely to cause KIE associated with degassing because solution pH is controlled by titrants, rather than passive pH control by sparging with N_2 to degas CO_2 from solution. Degassing can occur in the constant composition-style experiments presented here because the high supersaturation required for siderite nucleation is far from equilibrium with the CO_2-free atmosphere in the vessel headspace at the experiment outset. With a properly-sealed vessel, (that is, sealing the vessel-rim contact with silicone vacuum grease and reinforcing port seals), the volume of CO_2 that can degas from solution at our experimental temperatures is small relative to the residual precipitating solution DIC. Thus, a possible advantage of constant composition experiments in siderite is that this method can aid in fully disentangling KIE related to degassing from those related to growth rate and saturation state. For example, in calcite constant composition experiments, there was no observed correlation between growth rate and Δ_{47} (Levitt et al., 2018); however, both $\delta^{13}C$ (temperature-independent) and $\delta^{18}O$ (temperature-dependent) fractionation were found to be a function of growth rate. In contrast, an inverse relation between saturation state and Δ_{47} was found, indicating that calcites formed at high supersaturation are likely to be furthest from equilibrium Δ_{47} values. In addition to minimizing degassing, our method allows for a large volume of precipitate (10-20 grams on average) to be formed on relatively short timescales. This is beneficial for applications requiring more than a few milligrams of material. Our results also show that this method is relatively successful in promoting and maintaining siderite precipitation at a set pH and temperature (Fig. 2). Although not all experiments were considered chemostatic,

pH excursions exceeding ±1 pH unit did not occur and did not affect our ability to form siderite at all experimental temperatures.

As described in previous sections, pH control in our application of this method was affected by the occurrence of "runaway" titrant additions in roughly half of our experiments (Table 1). In these cases, we hypothesize that the titration software occasionally has difficulty recovering from the initial period of siderite precipitation once K_{crit} is reached, which causes pH to fluctuate quickly for a brief period of time. In non-chemostatic experiments, this fluctuation resulted in runaway titrant addition that initiated early in some experiments. Experiments where runaway events occurred during the initial nucleation event were more likely to experience subsequent runaway events as the experiment progressed, perhaps as a result of the rapid initial drawdown of Fe and DIC, followed by subsequent buildup to another precipitation "event", which caused further pH instability. Despite these challenges, our isotope results, discussed in section 4.3 (below), show that the lack of chemostasis does not appear to have a major impact on precipitate $\delta^{13}C$, $\delta^{18}O$, or Δ_{47}.

4.1.2. Homogeneous Nucleation vs. Seeded Growth Using This Method

Experimental siderite precipitation has two potential pathways through which the crystalline precipitate may be formed: homogeneous nucleation, in which carbonate precipitates spontaneously from the working solution (Wiesli et al., 2004; Fernandez et al., 2014; Jiang and Tosca, 2019; van Dijk et al., 2019), and seeded growth, in which seed crystals (often powder of a specific, homogeneous grain size) are placed in the reactor at the experiment outset (Levitt et al., 2018; Jiang and Tosca, 2020). We hypothesize that the long duration of our experiments resulted in a stepped siderite growth pathway that involved both homogeneous nucleation and seeded growth based on our visual observations of precipitation throughout the progress of experiments.

The homogeneous nucleation phase of our experiments began when K_{crit} was reached, at which point we observed that the working solution would become slightly cloudy or opaque due to the presence of a light-colored precipitate; typically, this was observed during the initial $FeCl_2$ injections, just before the target [Fe^{2+}] was reached. The timing of the initial nucleation phase appeared to vary with temperature, with precipitation beginning earlier as the temperature increased. Following this initial nucleation, the remainder of the experiment may be considered a seeded growth phase, during which it seems likely that the Fe-carbonate formed during the initial nucleation period acted as a seed material for new growth. Given that the autotitrator continued to make adjustments to the solution chemistry in response to continued precipitation, we assume this regime persisted until experiment termination.

4.2 Comparison of Carbon and Oxygen Isotopes with Previous Studies

Whether or not equilibrium precipitation was attained during our experiments can be further evaluated by comparison of $\delta^{13}C$ and $\delta^{18}O$ values with those of previous siderite laboratory synthesis and calibration studies. Figure 8 shows calculated carbon isotope fractionation factors ($\varepsilon_{FeCO3\text{-}HCO3\text{-}}$) at each experimental temperature for this study, as well as siderite values from Jiang et al. (2022) and calcites reported in Romanek et al. (1992). Fractionation between siderite and HCO_3^- from our experimental precipitates is indistinguishable from that of calcite (Romanek, 1992), suggesting that carbon isotope fractionation between carbonate and DIC is similar between carbonate mineralogies that share many crystallographic similarities and may likewise precipitate through an amorphous carbonate intermediate (Dideriksen et al., 2015; Jiang & Tosca, 2019). Over a range of precipitation temperatures relevant to Earth surface conditions we find no temperature dependence of carbon isotope fractionation.

Our precipitated siderite oxygen isotope values are generally consistent with previously reported values of laboratory precipitates and some natural siderite samples (Fig. 9). Not shown in Figure 9 are chukanovite-bearing samples that are offset from predicted siderite values for a given temperature by ~−2 to −4‰. We hypothesize that this is related to KIE, which we discuss further in Section 4.3. Combining oxygen isotope data from siderite precipitates from our experiments, Carothers et al. (1988), Zhang et al. (2001), Fernandez et al. (2014), and van Dijk et al. (2018) yields a best-fit equation of:

$$(5)\ 1000\ln^{18}\alpha = 18.07\ (\pm 0.71) * \frac{10^3}{T} - 29.92\ (\pm 2.23)$$

where T is the temperature in Kelvin, with an $R^2 = 0.946$ (Fig. 9). This relationship is valid from 8.5 to 200 °C. The agreement of our samples with previously published oxygen isotope ratios suggests that pure siderites precipitated using our constant compositions method were formed at oxygen isotope equilibrium. However, it is also possible that the correlation of our results with those of previously published samples is a consequence of oxygen isotope disequilibrium in all experiments, potentially as a result of ^{18}O fractionation associated with high precipitation rates and high supersaturation levels required for siderite precipitation (Levitt et al., 2018). We contend that this seems unlikely given the agreement between synthetic samples and natural siderites, and the overlap between constant composition (this study), active degassing (Fernandez et al., 2014; van Dijk et al., 2018), microbially-mediated (Zhang et al., 2001), and hydrothermal (Carothers et al., 1988) precipitation methods at ~50 °C. It may be that the apparent variability in Figure 9 is related to unrecognized and understudied methodological differences in siderite acid digestion, for example, 60 min reactions at 90 °C in a common acid bath in which CO_2 was actively trapped (Section 2.3) versus ~30 min reactions at 100 °C in McCrea-type reaction vessels in Fernandez et al. (2014). The slow kinetics of siderite dissolution relative to other

carbonates (Al-Aasm et al., 1990), like calcite and dolomite, may amplify these interlaboratory differences.

4.3 Towards a composite siderite clumped isotope calibration

Given the agreement of our oxygen isotope data with all previous attempts to calibrate the siderite-water oxygen isotope thermometer (Fig. 9), and an apparent agreement between published siderite precipitate Δ_{47} and our new data (Fig. 10A), we propose a new composite calibration curve using all published siderite data (Fig. 12). As with Equation 5, chukanovite-bearing samples from this study were excluded from the regression. This line has the equation:

$$(6)\ \Delta_{47} = \frac{0.0364(\pm 0.004) \times 10^6}{T^2} + 0.1672(\pm 0.046)$$

where T ranges from 8.5-75°C. The slope of this regression is indistinguishable from the Petersen et al. (2019) composite calibration (which includes data from Fernandez et al. (2014)) but is ~0.09‰ lower in its y-intercept. This offset from the composite calibration, which is populated dominantly by calcium carbonates, is obvious in Figure 12 and was first identified by van Dijk et al. (2019).

The apparent concordance between our data and that from Fernandez et al. (2014) and van Dijk et al. (2019) may support one of two hypotheses: first, despite the potential issues we raised with respect to KIE associated with degassing during the active degassing methods employed in prior siderite calibration studies (Section 4.1.1), degassing did not affect the clumped isotope composition of precipitates from any of the three datasets; conversely, the agreement between the three datasets may indicate that all three of our experimental methods were significantly compromised by degassing, with the effect being of roughly equivalent

magnitude in all three cases, conspiring to produce a consistent set of data across the three studies.

To investigate the possibility that all siderite synthesis experiments were compromised by degassing KIEs, we show all published experimental siderite Δ_{47} data with Δ_{47} data from natural siderites formed at well-constrained temperatures (full description of samples are given in van Dijk et al. (2019)) in Figure 10A. Data from these natural siderites is in agreement with the experimental data, which may suggest that the offset of siderite data from carbonate compilation regressions like that of Petersen et al. (2019) is an inherent feature of siderite Δ_{47}, rather than an artifact of laboratory synthesis. One such feature could be a difference in the acid fractionation factor (AFF) between siderite and other carbonates like calcite and dolomite. This has been suggested by theoretical studies of carbonate AFF (e.g., Guo et al., 2009) but, unlike calcite and dolomite (Passey and Henkes, 2012; Lloyd et al., 2018), has not been confirmed empirically by the heating of siderites to a range of high temperatures where equilibrium ^{13}C-^{18}O bond ordering should be achieved on laboratory timescales and thus Δ_{47} known *a priori*. Nevertheless, siderite AFF, at least relative to other carbonate minerals, is virtually unknown.

A single siderite heating experiment at 625 °C, described in Section 2.2., was conducted as a test of possible differences in AFF between siderite and other carbonate minerals, and thus a test whether AFF may explain the offsets observed in Figures 10 & 12. The Δ_{47} of the heated siderite sample, 0.206 ± 0.006‰ (±1 SE), is statistically indistinguishable from the value predicted by Eqn. 1 of Petersen et al. (2019) for a carbonate at 625°C (Δ_{47} = 0.217‰). To evaluate these values, we combined the predicted value for a carbonate at 625°C and the error for data that corresponds to a temperature above 300°C in the curve shown in Figure 4B of Petersen

et al. (2019) and applied those values in a Student's T-test (1σ SE = 0.016, n = 6). The p value was 0.16, which precludes significance at any reasonable level. Furthermore, the calcitic interlaboratory standards ETH-1 and ETH-2 (Bernasconi et al., 2018; 2021) were both heated to 600 °C, just 25 °C cooler than our own experiment. Bernasconi et al (2021) report values of 0.205 and 0.208‰, respectively (for an acid reaction temperature of 90 °C), virtually indistinguishable from our heated siderite value. Based on this comparison, we hypothesize that AFF differences are not the cause of the offset between siderite data and published composite calibrations populated mostly by calcium carbonates and dolomite. However, this conclusion is tentative because it is based on a single siderite heating experiment and further investigation is needed to fully characterize the siderite. Nevertheless, the offsets seen in Figures 10 & 12 are conspicuous and of sufficient magnitude (~-0.05‰) to necessitate an explanation that will guide the use of an appropriate temperature calibration as applied in paleothermometry of natural siderite samples. Next, we consider the consequences of isotope effects during our siderite precipitation experiments as a driver of Δ_{47} offsets.

4.4 Possible Precipitation Controls on Siderite Δ_{47}

We have identified four inter-related experimental considerations that are likely to affect isotope ratios of our experimentally precipitated Fe-carbonates: (1) sealing of the vessel, (2) degree of experimental control, (3) saturation index/precipitation rate, and (4) Fe:DIC ratio.

A sealed or unsealed vessel may impact isotope ratios of the precipitates due to KIE associated with water evaporation and CO_2 degassing (Guo, 2008; Affek and Zaarur, 2014). In our experiments, an improperly sealed vessel allowed for exchange between the glovebox atmosphere and reaction vessel headspace (*e.g.* 75-1A), which can cause an increase $\delta^{18}O_{DIC}$ of the working solution by degassing of CO_2 and/or evaporative distillation of ^{18}O in the residual

fluid. Furthermore, regardless of the vessel seal, the headspace is not initially at pCO_2 equilibrium with the working solution, which may naturally promote CO_2 degassing into the headspace in the initial minutes to hours of an experiment. It is therefore conceivable that KIE associated with the dehydration/dehydroxylation of HCO_3^- can be inherited by siderite formed at the surface of the working solution even in well-sealed experiments. We do not believe, however, that this constituted a significant control on Δ_{47} of the resulting precipitate; Figure 10B shows that a sealed or unsealed vessel displays little correlation with Δ_{47} value, or where precipitate $\delta^{18}O$ and Δ_{47} fall with respect to the predicted equilibrium curves of van Dijk et al. (2018, 2019). The exception to this rule was 75-1A, which was significantly impacted by evaporation due to an improperly sealed vessel; this point is clearly separated from the rest of the data. However, for all other experiments (none of which were noticeably compromised by evaporation), we do not find evidence to support that sealing the vessel has a measurable impact on Δ_{47} composition in our experiments.

Next, the degree of experimental control (*i.e.*, chemostatic vs. non-chemostatic) may influence the isotope ratio of siderite precipitates. This may happen for multiple reasons. First, the degree of experimental control directly correlates with the ability to maintain a set pH for siderite saturation. Significant excursions (*i.e.*, > 0.1pH unit but <1 pH unit) from a set point, though rare even in non-chemostatic experiments, can cause deviation from this. In our experimental setup this would result in either higher siderite saturation if the DIC titrant is added in a runaway event or in lower siderite saturation if Fe^{2+} titrant is added in a runaway event. Additionally, titrants added uncontrollably can cause similar effects on siderite saturation by increasing the activity of either Fe^{2+} or DIC. In theory, the combination of pH change and activity change may result in rapid siderite precipitation. However, Figure 10B also shows that

degree of experimental control does not appear to strongly correlate with Δ_{47} value. This is likely because the pH excursions in non-chemostatic experiments were not large or long enough in duration to cause a significant shift in siderite phase space (Fig. 7) that resulted in either rapid precipitation or dissolution. Additionally, degree of experimental control does not correlate with chukanovite formation, which further indicates that runaway titrant additions were not significant enough to shift the experiment away from siderite saturation.

We hypothesize that saturation index (SI) could be a strong control on the clumped isotope ratio of siderite precipitates because of its relationship to precipitation rate, which has been shown to cause KIE when precipitation is rapid (Watkins and Hunt, 2015; Levitt et al., 2018). Because our experiments were conducted at a high saturation (Fig. 7), it is conceivable that rapid nucleation when K_{crit} was reached resulted in KIE in our precipitates. Additionally, SI may be an important control on Δ_{47} due to its influence on siderite growth rate; recent studies have demonstrated that rapid growth rates under supersaturated conditions may result in KIEs for both Δ_{47} (Levitt et al., 2018) and $\delta^{13}C$ (Jiang et al., 2022). Tables 1 & 2 present saturation index and Δ_{47} for all measured precipitates, respectively. There is no obvious correlation between SI and Δ_{47}. Within the limits of our data, we do not know how the mass of siderite precipitation was distributed with respect to time, and therefore we must assume that siderite isotope ratios represent a time-average throughout the experimental duration. This simple assumption is important because Jiang et al. (2022) posit that homogeneous nucleation and crystal growth in the Fe-carbonate system each have distinct KIE, and thus it is possible that the isotope ratios of the precipitates formed in this study represent mixing between these separate fractionations. Additionally, the range of saturation indices calculated for our experiments is relatively small (from ~1-3), making potential differences in isotope ratios proportionally small. For these

reasons, it is possible that our measured isotope ratios were impacted by SI effects, but we cannot definitively conclude that these are the primary control. Importantly, we note that the agreement in stable isotope ratios between our precipitates, previous experimental studies, and natural samples suggests that any SI effects observed in our samples are inherent to siderite, rather than an artifact of the experimental methods.

The final potential control on experimental siderite Δ_{47} is the Fe:DIC ratio. There are two possible pathways that this ratio could affect the Δ_{47}: (1) the high DIC necessary for pure siderite nucleation creates a high SI, potentially leading to KIE associated with rapid precipitation and (2) Fe:DIC has been shown to be a controlling factor in which Fe-carbonate phase recrystallizes from AFC (*i.e.*, siderite or chukanovite; Jiang & Tosca, 2019; Koo & Kim, 2020). Because SI controls were discussed above, in this section, we will discuss Fe:DIC as it relates to Fe-carbonate phases as a potential control of isotope ratios of the precipitates. As we have identified (Section 3.3), the chukanovite-bearing samples (15-1C, 25-1A and 50-4C) depart significantly from the rest of our samples in $\delta^{18}O$ and Δ_{47} (Figs. 9 & 10). For example, chukanovite-bearing samples plot to the upper left relative to data from pure siderite, which plot on or within error of the equilibrium curve from van Dijk et al. (2018 and 2019). To evaluate the cause of this offset, we normalize the Δ_{47} and 1000lnα values of all published synthetic siderite values to the predicted equilibrium values derived from our calculated Δ_{47} and 1000lnα regressions (Equations 5 & 6, respectively) and superimposed these normalized values on vectors that represent the expected directional shift from disequilibrium KIE associated with CO_2 hydration and hydroxylation, *i.e.*, CO_2 (aq) + $H_2O \rightarrow HCO_3^-$ + H^+, and CO_2 (aq) + $OH^- \rightarrow HCO_3^-$, respectively (Fig. 13; Falk et al*.,* 2016), and shown to exist in carbonates formed in alkaline springs (Clark et al., 1992; Falk et al., 2016). Recent work by Uchikawa et al. (2021)

constrains the time-dependent approach to oxygen and clumped isotope equilibrium resulting from CO_2 hydration and hydroxylation reactions. In all of these cases, the KIE in question relate to effects associated with the equilibration of the isotopic composition of DIC (specifically in the form of $CO_{2,\,aq}$) and the water reservoir it is dissolved in, and these KIEs should be eliminated by equilibrating over ~24-36 hours before starting a carbonate precipitation experiment (Uchikawa et al., 2021). In fact, we took precautions to eliminate such KIEs at the outset of all of our experiments by allowing DIC-water equilibration to take place for 24 hours prior to the initial titrant injection. Despite this, the samples containing chukanovite appear consistent with disequilibrium isotope effects from hydroxylation and/or hydration reactions (Fig. 13). We speculate that the Fe:DIC ratio of the fluid, and its control on the nature of the Fe-carbonate precipitates that form from it, result in isotope values that appear to be affected by hydration/hydroxylation KIEs, perhaps occurring during the recrystallization of AFC to chukanovite. Ascribing the chukanovite-bearing sample isotope ratios to a known KIE-inducing mechanism strengthens our confidence in the isotope values of the precipitated siderite that conforms with previous experiments. However, this offers little guidance for the observed Δ_{47} differences because siderite Δ_{47} is low with respect to composite clumped isotope temperature calibrations (Fig. 12) despite carbonate $\delta^{18}O$ agreeing with established siderite-water equilibrium relationships (Fig. 9). Kinetic isotope effects associated with CO_2 dehydration and dehydroxylation are equal and opposite to the effects just described, which would be the correct sign to explain the problematic siderite Δ_{47} offset but would also predict $\delta^{18}O$ changes on the order of several ‰ that are not observed.

5. Conclusion

We present carbonate isotope results for siderite experimentally precipitated at 15-75°C and evaluate our experimental data with previous studies that have also presented calibrations of siderite-water oxygen isotope and clumped isotope thermometry. We demonstrate that a modified constant composition method is successful in precipitating siderite at temperatures as cool at 15 °C, with isotope values that generally agree with published experimental studies of equilibrium isotope fractionation. This method allows us to differentiate between degassing and supersaturation-related kinetic isotope effects, and we hypothesize that Fe:DIC ratio is an important determinant of isotope ratios in our precipitates due to its influence on whether our precipitates consisted of siderite or siderite+chukanovite. We show through a successful siderite heating experiment that the AFF of siderite is likely indistinguishable to that of Ca- and Mg-carbonates, though more such experiments are needed to constrain this coherence. It is possible that kinetic effects related to high supersaturation contribute to this offset and future experiments should more systematically investigate the effect of supersaturation on isotopic composition. The agreement between synthetic and natural siderite clumped isotope data indicates that the observed differences in clumped isotope between siderite and other carbonates may be inherent to siderite precipitation, rather than a shortcoming of laboratory synthesis methods. We suggest that a siderite-specific temperature calibration may be necessary, but caution against the application of current siderite calibrations in natural samples until the cause of these isotope differences are better understood.

Acknowledgements

We would like to thank Katie Wooton, David Burtt, and Victoria Rivera-Banuchi for their assistance in multiple Stony Brook Geoscience laboratories; Andy Knoll for providing the Mazon Creek siderite nodule for use as a working standard during stable isotope analyses; Clancy Zhijian Jiang for his helpful discussions; and Jacob Jordan for his assistance with data visualization. We thank two anonymous reviewers and associate editor Shuhei Ono for their helpful comments that improved this manuscript. This work was supported by the Simons Collaboration on the Origin of Life award number 572786 (J.A.H.) and Stony Brook University start-up funds (G.A.H).

Appendix A: Supplementary Material

Supplementary material for this article includes the raw data for stable isotope analyses and starting conditions for all experiments, as well as the XRD pattern of the heated siderite sample.

References

Affek H. P. (2013) Clumped isotopic equilibrium and the rate of isotope exchange between CO2 and water. *Am. J. Sci.* **313**, 309–325.

Affek H. P. and Zaarur S. (2014) Kinetic isotope effect in CO2 degassing: Insight from clumped and oxygen isotopes in laboratory precipitation experiments. *Geochim. Cosmochim. Acta* **143**, 319–330.

Al-Aasm I. S., Taylor B. E. and South B. (1990) Stable isotope analysis of multiple carbonate samples using selective acid extraction. *Chem. Geol.* **80**, 119–125.

Anderson N. T., Kelson J. R., Kele S., Daëron M., Bonifacie M., Horita J., Mackey T. J., John C. M., Kluge T. and Petschnig P. (2021) A unified clumped isotope thermometer calibration (0.5–1,100 C) using carbonate-based standardization. *Geophys. Res. Lett.* **48**, e2020GL092069.

Beck R., Seiersten M. and Andreassen J. P. (2013) The constant composition method for crystallization of calcium carbonate at constant supersaturation. *J. Cryst. Growth* **380**, 187–196.

Bernasconi, S.M., Müller, I.A., Bergmann, K.D., Breitenbach, S.F., Fernandez, A., Hodell, D.A., Jaggi, M., Meckler, A.N., Millan, I. and Ziegler, M. (2018) Reducing uncertainties in carbonate clumped isotope analysis through consistent carbonate-based standardization. *Geochem, Geophys, Geosys*, **19**, 2895-2914.

Bernasconi, S.M., Daëron, M., Bergmann, K.D., Bonifacie, M., Meckler, A.N., Affek, H.P., Anderson, N., Bajnai, D., Barkan, E., Beverly, E., Blamart, D., Burgener, L., Calmels, D., Chaduteau, C., Clog, M., Davidheiser-Kroll, B., Davies, A., Dux, F., Eiler, J., Elliot, B., Fetrow, A.C., Fiebig, J., Goldberg, S., Hermoso, M., Huntington, K.W., Hyland, E., Ingalls, M., Jaggi, M., John, C.M., Jost, A.B., Katz, S., Kelson, J., Kluge, T., Kocken, I.J., Laskar, A., Leutert, T.J., Liang, D., Lucarelli, J., Mackey, T.J., Mangenot, X., Meinicke, N., Modestou, S.E., Müller, I.A., Murray, S., Neary, A., Packard, N., Passey, B.H., Pelletier, E., Petersen, S., Piasecki, A., Schauer, A., Snell, K.E., Swart, P.K., Tripati, A, Upadhyay, D., Vennemann, T., Winkelstern, I., Yarian, D., Yoshida, N., Zhang, N., and Ziegler, M. (2021) InterCarb: A community effort to improve interlaboratory standardization of the carbonate clumped isotope thermometer using carbonate standards. *Geochem., Geophys., Geosys.*, **22**.

Bonifacie M., Calmels D., Eiler J. M., Horita J., Chaduteau C., Vasconcelos C., Agrinier P., Katz A., Passey B. H., Ferry J. M. and Bourrand J. J. (2017) Calibration of the dolomite clumped isotope thermometer from 25 to 350 °C, and implications for a universal calibration for all (Ca, Mg, Fe)CO3 carbonates. *Geochim. Cosmochim. Acta* **200**, 255–279.

Carothers W. W., Adami L. H. and Rosenbauer R. J. (1988) Experimental oxygen isotope fractionation between siderite-water and phosphoric acid liberated CO2-siderite. *Geochim. Cosmochim. Acta* **52**, 2445–2450.

Dennis K. J., Affek H. P., Passey B. H., Schrag D. P. and Eiler J. M. (2011) Defining an absolute reference frame for "clumped" isotope studies of CO2. *Geochim. Cosmochim. Acta* **75**, 7117–7131.

Dideriksen K., Frandsen C., Bovet N., Wallace A. F., Sel O., Arbour T., Navrotsky A., de Yoreo J. J. and Banfield J. F. (2015) Formation and transformation of a short range ordered iron carbonate precursor. *Geochim. Cosmochim. Acta* **164**, 94–109.

van Dijk J., Fernandez A., Müller I. A., Lever M. and Bernasconi S. M. (2018) Oxygen isotope fractionation in the siderite-water system between 8.5 and 62 °C. *Geochim. Cosmochim. Acta* **220**, 535–551.

van Dijk J., Fernandez A., Storck J. C., White T. S., Lever M., Müller I. A., Bishop S., Seifert R. F., Driese S. G., Krylov A., Ludvigson G. A., Turchyn A. v., Lin C. Y., Wittkop C. and Bernasconi S. M. (2019) Experimental calibration of clumped isotopes in siderite between 8.5 and 62 °C and its application as paleo-thermometer in paleosols. *Geochim. Cosmochim. Acta* **254**, 1–20.

Eiler J. M. (2007) "Clumped-isotope" geochemistry—The study of naturally-occurring, multiply-substituted isotopologues. *Earth Planet Sci. Lett.* **262**, 309–327.

Falk E. S., Guo W., Paukert A. N., Matter J. M., Mervine E. M. and Kelemen P. B. (2016) Controls on the stable isotope compositions of travertine from hyperalkaline springs in Oman: Insights from clumped isotope measurements. *Geochim. Cosmochim. Acta* **192**, 1–28.

Fernandez A., Tang J. and Rosenheim B. E. (2014) Siderite "clumped" isotope thermometry: A new paleoclimate proxy for humid continental environments. *Geochim. Cosmochim. Acta* **126**, 411–421.

Floran R. J. and Papike J. J. (1978) Mineralogy and petrology of the Gunflint Iron Formation, Minnesota-Ontario: correlation of compositional and assemblage variations at low to moderate grade. *J. Pet.* **19**, 215–288.

French B. M. (1973) Mineral assemblages in diagenetic and low-grade metamorphic iron-formation. *Econ. Geol.* **68**, 1063–1074.

Galili N., Shemesh A., Yam R., Brailovsky I., Sela-Adler M., Schuster E. M., Collom C., Bekker A., Planavsky N., Macdonald F. A., Préat A., Rudmin M., Trela W., Sturesson U., Heikoop J. M., Aurell M., Ramajo J. and Halevy I. (2019) The geologic history of seawater oxygen isotopes from marine iron oxides. *Science 365* **6542**, 469-473.

Ghosh P., Adkins J., Affek H., Balta B., Guo W., Schauble E. A., Schrag D. and Eiler J. M. (2006) 13C-18O bonds in carbonate minerals: A new kind of paleothermometer. *Geochim. Cosmochim. Acta* **70**, 1439–1456.

Guo W. (2008) Carbonate clumped isotope thermometry: application to carbonaceous chondrites & effects of kinetic isotope fractionation. Ph.D. Thesis, CalTech, USA.

Guo W., Mosenfelder J. L., Goddard W. A. and Eiler J. M. (2009) Isotopic fractionations associated with phosphoric acid digestion of carbonate minerals: Insights from first-principles theoretical modeling and clumped isotope measurements. *Geochim. Cosmochim. Acta* **73**, 7203–7225.

Halevy I., Fischer W. W. and Eiler J. M. (2011) Carbonates in the Martian meteorite Allan Hills 84001 formed at 18 AE 4 °C in a near-surface aqueous environment. *Proc. Nat. Ac. Sci.* **108**, 16895–16899.

Harvey R. P. and McSween H. Y. (1996) A possible high-temperature origin for the carbonates in the Martian meteorite ALH84001. *Nature* **382**, 49–51.

Helgeson H. C. (1978) Summary and critique of the thermodynamic properties of rock-forming minerals. *Am. J. Sci.* **278**, 1–229.

Helgeson H C (1969) Thermodynamics of hydrothermal systems at elevated temperatures and pressures. *Am. J. Sci.* **267**, 729–804.

Helgeson H. C. (1969) Thermodynamics of hydrothermal systems at elevated temperatures and pressures. *Am. J. Sci.* **267**, 729–804.

Helgeson H. C. and Kirkham D. H. (1974) Theoretical prediction of the thermodynamic behavior of aqueous electrolytes at high pressures and temperatures; I, Summary of the thermodynamic/electrostatic properties of the solvent. *Am. J. Sci.* **274**, 1089–1198.

Henkes G. A., Passey B. H., Grossman E. L., Shenton B. J., Yancey T. E. and Pérez-Huerta A. (2018) Temperature evolution and the oxygen isotope composition of Phanerozoic oceans from carbonate clumped isotope thermometry. *Earth and Planet. Sci. Lett.* **490**, 40–50.

Holland H. D. (1984) The Chemical Evolution of the Oceans and Atmosphere. Princeton University Press, Princeton.

Horgan B. H. N., Anderson R. B., Dromart G., Amador E. S. and Rice M. S. (2020) The mineral diversity of Jezero crater: Evidence for possible lacustrine carbonates on Mars. *Icarus* **339,** 113526.

Huntington K. W., Eiler J. M., Affek H. P., Guo W., Bonifacie M., Yeung L. Y., Thiagarajan N., Passey B., Tripati A., Daëron M. and Came R. (2009) Methods and limitations of "clumped" CO2 isotope (Δ47) analysis by gas-source isotope ratiomass spectrometry. *J. Mass Spectrom.* **44**, 1318–1329.

Jiang C. Z., Halevy I. and Tosca N. J. (2022) Kinetic isotope effect in siderite growth: Implications for the origin of banded iron formation siderite. *Geochim. Cosmochim. Acta* **322**, 260–273.

Jiang C. Z. and Tosca N. J. (2019) Fe(II)-carbonate precipitation kinetics and the chemistry of anoxic ferruginous seawater. *Earth and Planet. Sci. Lett.* **506**, 231–242.

Jiang C. Z. and Tosca N. J. (2020) Growth kinetics of siderite at 298.15 K and 1 bar. *Geochim. Cosmochim. Acta* **274**, 97–117.

Johnson J. W., Oelkers E. H. and Helgeson H. C. (1992) SUPCRT92: A software package for calculating the standard molal thermodynamic properties of minerals, gases, aqueous species, and reactions from 1 to 5000 bar and 0 to 1000 C. *Comp. & Geosci.* **18**, 899–947.

Kang N., Schmidt M. W., Poli S., Franzolin E. and Connolly J. A. D. (2015) Melting of siderite to 20GPa and thermodynamic properties of FeCO3-melt. *Chem. Geol.* **400**, 34–43.

Kazmierczak T. F., Tomson M. B. and Nancollas G. H. (1982) Crystal growth of calcium carbonate. A controlled composition kinetic study. *J. Phys. Chem.* **86**, 103–107.

Kim, S.T. and O'Neil, J. R. (1997) Equilibrium and nonequilibrium oxygen isotope effects in synthetic carbonates. *Geochim. Cosmochim. Acta* **61**, 3461-3475.

Klein C. (1973) Changes in mineral assemblages with metamorphism of some banded Precambrian iron-formations. *Econ. Geol.* **68**, 1075–1088.

Klein C. (2005) Some Precambrian banded iron-formations (BIFs) from around the world: Their age, geologic setting, mineralogy, metamorphism, geochemistry, and origin. *Am. Mineralogist* **90**, 1473–1499.

Kluge T., Affek H. P., Marx T., Aeschbach-Hertig W., Riechelmann D. F. C., Scholz D., Riechelmann S., Immenhauser A., Richter D. K. and Fohlmeister J. (2013) Reconstruction of drip-water δ 18 O based on calcite oxygen and clumped isotopes of speleothems from Bunker Cave (Germany). *Climate of the Past* **9**, 377–391.

Konhauser K. O., Planavsky N. J., Hardisty D. S., Robbins L. J., Warchola T. J., Haugaard R., Lalonde S. v., Partin C. A., Oonk P. B. H., Tsikos H., Lyons T. W., Bekker A. and Johnson C. M. (2017) Iron formations: A global record of Neoarchaean to Palaeoproterozoic environmental history. *Earth-Sci. Rev.* **172**, 140–177.

Koo T. H. and Kim J. (2020) Controls on the formation and stability of siderite (FeCo3) and chukanovite (Fe2(CO3)(OH)2) in reducing environment. *Minerals* **10**.

Koutsoukos P., Amjad Z., Tomson M. B. and Nancollas G. H. (1980) Crystallization of calcium phosphates. A constant composition study. *J. Am. Chem. Soc.* **102**, 1553–1557.

Clark, I.D. and Lauriol, B. (1992) Kinetic enrichment of stable isotopes in cryogenic calcites. *Chem. Geol.* **102**, 217-228.

Levitt N. P., Eiler J. M., Romanek C. S., Beard B. L., Xu H. and Johnson C. M. (2018) Near Equilibrium ^{13}C - ^{18}O Bonding During Inorganic Calcite Precipitation Under Chemo-Stat Conditions. *Geochem., Geophys., Geosys.***19**, 901–920.

Lewis G. N., Randall M., Pitzer K. S. and Brewer L. (2020) *Thermodynamics*., Courier Dover Publications.

Lindskog S. and Coleman J. E. (1973) The catalytic mechanism of carbonic anhydrase. *Pro. Nat. Ac. Sci.* **70**, 2505–2508.

Lloyd M. K., Ryb U. and Eiler J. M. (2018) Experimental calibration of clumped isotope reordering in dolomite. *Geochim. Cosmochim. Acta* **242**, 1–20.

Ludvigson G. A., González L. A., Fowle D. A., Roberts J. A., Driese S. G., Villarreal M. A., Smith J. J. and Suarez M. B. (2013) Paleoclimatic applications and modern process studies of pedogenic siderite. *SEPM Spec. Pub.* **104**, 79–87.

Morris R. v, Ruff S. W., Gellert R., Ming D. W., Arvidson R. E., Clark B. C., Golden D. C., Siebach K., Klingelhöfer G. and Schröder C. (2010) Identification of carbonate-rich outcrops on Mars by the Spirit rover. *Science (1979)* **329**, 421–424.

Mucci A. and Morse J. W. (1983) The incorporation of Mg^{2+} and Sr^{2+} into calcite overgrowths: influences of growth rate and solution composition. *Geochim. Cosmochim. Acta* **47**, 217–233.

Passey B. H. and Henkes G. A. (2012) Carbonate clumped isotope bond reordering and geospeedometry. *Earth and Planet. Sci. Lett.* **351–352**, 223–236.

Petersen S. v., Defliese W. F., Saenger C., Daëron M., Huntington K. W., John C. M., Kelson J. R., Bernasconi S. M., Colman A. S., Kluge T., Olack G. A., Schauer A. J., Bajnai D., Bonifacie M., Breitenbach S. F. M., Fiebig J., Fernandez A. B., Henkes G. A., Hodell D., Katz A., Kele S., Lohmann K. C., Passey B. H., Peral M. Y., Petrizzo D. A., Rosenheim B. E., Tripati A., Venturelli R., Young E. D. and Winkelstern I. Z. (2019) Effects of Improved 17O Correction on Interlaboratory Agreement in Clumped Isotope Calibrations, Estimates of Mineral-Specific Offsets, and Temperature Dependence of Acid Digestion Fractionation. *Geochem., Geophys., Geosys.* **20**, 3495–3519.

Poulsen C. J., Pollard D. and White T. S. (2007) General circulation model simulation of the δ18O content of continental precipitation in the middle Cretaceous: A model-proxy comparison. *Geology* **35**, 199–202.

Romanek, C.S., Grossman, E.L. and Morse, J.W. (1992) Carbon isotopic fractionation in synthetic aragonite and calcite: effects of temperature and precipitation rate. *Geochim. Cosmochim. Acta* **56**, 419-430.

Rosenbaum J. and Sheppard S. M. F. (1986) An isotopic study of siderites, dolomites and ankerites at high temperatures. *Geochim. Cosmochim. Acta* **50**, 1147–1150.

Ryb U. and Eiler J. M. (2018) Oxygen isotope composition of the Phanerozoic ocean and a possible solution to the dolomite problem. *Pro. Nat. Ac. Sci.* **115**, 6602–6607.

Schauble E. A., Ghosh P. and Eiler J. M. (2006) Preferential formation of ^{13}C-^{18}O bonds in carbonate minerals, estimated using first-principles lattice dynamics. *Geochim. Cosmochim. Acta* **70**, 2510–2529.

Shaojun, Z. and Mucci, A. (1993) Calcite precipitation in seawater using a constant addition technique: A new overall reaction kinetic expression. *Geochim. Cosmochim. Acta* **57**, 1409-1417.

Singer, P.C. and Stumm, W. (1970) The solubility of ferrous iron in carbonate-bearing waters. *J. Am. Water Works Assoc.* **62**, 198-202.

Spanos, N. and Koutsoukos, P.G. (1998) Kinetics of precipitation of calcium carbonate in alkaline pH at constant supersaturation. Spontaneous and seeded growth. *J. Phys. Chem. B* **102**, 6679-6684.

Tang R., Henneman Z. J. and Nancollas G. H. (2003) Constant composition kinetics study of carbonated apatite dissolution. *J. Cryst. Growth* **249**, 614–624.

Tice, M.M., Hurowitz, J.A., Allwood, A.C., Jones, M.W., Orenstein, B.J., Davidoff, S., Wright, A.P., Pedersen, D.A., Henneke, J., Tosca, N.J., Moore, K.R., Clark, B.C., McLennan, S.M., Flannery, D.T., Steele, A., Brown, A.J., Zorzano, M.-P., Hickman-Lewis, K., Liu, Y., VanBommel, S.J., Schmidt, M.E., Kizovski, T.V., Trelman, A.H., O'Neill, L., Falrén, A.G., Shuster, D.L., Gupta, S., and PIXL Team (2022) Alteration history of Séítah formation rocks inferred by PIXL x-ray fluorescence, x-ray diffraction, and multispectral imaging on Mars. *Sci. Adv.*, **8**.

Tosca N. J., Jiang C. Z., Rasmussen B. and Muhling J. (2019) Products of the iron cycle on the early Earth. *Free Radical Biol. and Med.* **140**, 138–153.

Uchikawa J., Chen S., Eiler J. M., Adkins J. F. and Zeebe R. E. (2021) Trajectory and timescale of oxygen and clumped isotope equilibration in the dissolved carbonate system under normal and enzymatically-catalyzed conditions at 25 °C. *Geochim. Cosmochim. Acta* **314**, 313–333.

van Geldern, R. and Barth, J.A., 2012. Optimization of instrument setup and post-run corrections for oxygen and hydrogen stable isotope measurements of water by isotope ratio infrared spectroscopy (IRIS). *Limn. and Ocean.: Methods* **10**, 1024-1036.

Watkins J. M. and Hunt J. D. (2015) A process-based model for non-equilibrium clumped isotope effects in carbonates. *Earth and Planet. Sci. Lett.* **432**, 152–165.

Westin K. J. and Rasmuson Å. C. (2005) Crystal growth of aragonite and calcite in presence of citric acid, DTPA, EDTA and pyromellitic acid. *J. Coll. Interface Sci.* **282**, 359–369.

White, T., González, L., Ludvigson, G. and Poulsen, C. (2001) Middle Cretaceous greenhouse hydrologic cycle of North America. *Geology* **29**, 363-366.

Wiesli R. A., Beard B. L. and Johnson C. M. (2004) Experimental determination of Fe isotope fractionation between aqueous Fe(II), siderite and "green rust" in abiotic systems. *Chem. Geol.* **211**, 343–362.

Wittkop C., Teranes J., Lubenow B. and Dean W. E. (2014) Carbon- and oxygen-stable isotopic signatures of methanogenesis, temperature, and water column stratification in Holocene siderite varves. *Chem. Geol.* **389**, 153–166.

Žák K., Radvanec M. and Grecula P. (2005) Siderite mineralization of the Gemericum Superunit (Western Carpathians, Slovakia): review and a revised genetic model [Ore Geology Reviews 24, 267–298]—a reply. *Ore Geol. Rev.* **26**, 173–180.

Zastrow A. M. and Glotch T. D. (2021) Distinct Carbonate Lithologies in Jezero Crater, Mars. *Geophys. Res. Lett.* **48**.

Zeebe R. E. and Wolf-Gladrow D. (2001) CO2 in seawater: equilibrium, kinetics, isotopes., Gulf Professional Publishing.

Zhang, C.L., Horita, J., Cole, D.R., Zhou, J., Lovley, D.R. and Phelps, T.J. (2001) Temperature-dependent oxygen and carbon isotope fractionations of biogenic siderite. *Geochim. Cosmochim. Acta* **65**, 2257-2271.

Zhong, S. and Mucci, A., 1989. Calcite and aragonite precipitation from seawater solutions of various salinities: Precipitation rates and overgrowth compositions. *Chem. Geol.* **78**, 283-299.

Zhu, Z., Aller, R.C. and Mak, J. (2002) Stable carbon isotope cycling in mobile coastal muds of Amapa, Brazil. *Cont. Shelf Res.* **22**, 2065-2079.

	Other Expt. Conditions			Expt. Target Values						Expt. Observed Values				
Sample	Chemostatic*	Sealed**	Duration (hrs)	Temp	I.S. (M)	Fe (M)	DIC (M)	pH	Fe:DIC	SI	Temp	pH	pH variation	XRD
15-1A	Y	N	24	15	0.485	0.002 5	0.25	8.5	0.010	1.390	14.8	8.494-8.578	0.084	Sid
15-1C	N	Y	24	15	0.352	0.002 5	0.04 5	8.8	0.056	1.152	14.7	8.703-8.803	0.1	Sid/Chk
15-2A	Y	Y	24	15	0.485	0.002 5	0.25	8.3	0.010	1.709	15.1	8.270-8.315	0.045	Sid
25-1A	N	N	72	25	0.595	0.005	0.1	8.5	0.050	1.746	25.7	8.486-8.632	0.146	Sid/Chk
25-1B	N	N	48	25	0.524	0.001	0.3	8.0	0.003	1.789	24.7	7.530-8.515	0.985	Sid
25-2A	N	N	36	25	0.524	0.001	0.3	8.5	0.003	2.007	25.1	7.994-8.744	0.75	Sid
25-3A	Y	Y	24	25	0.524	0.001	0.3	8.4	0.003	1.690	24.9	8.387-8.434	0.047	Sid
50-2A	N	N	48	50	0.473	0.001	0.3	8.8	0.003	2.105	49.1	8.441-8.881	0.44	Sid
50-3A	N	N	60	50	0.473	0.001	0.3	8.3	0.003	1.629	48.9	7.618-8.307	0.689	Sid
50-4C	Y	Y	48	50	0.422	0.001	0.01 5	7.9	0.067	0.737	48.9	7.836-7.912	0.076	Sid/Chk
75-1A***	N	N	24	75	0.558	0.001	0.25	8	0.004	1.617	72.1	8.092-8.563	0.471	Sid
75-2B	Y	Y	12	75	0.558	0.001	0.25	8.2	0.004	1.636	72.1	8.178-8.572	0.394	Sid

*Defined has having pH fluctuations of <0.1 units over the course of the experiment
**Defined by the presence or absence of vacuum grease on the vessel-lid contact
***Significant evaporative water losses were observed in this experiment

Table 1. Target and observed conditions for all experiments.

Sample	Count	$\delta^{13}C_c$	$\delta^{13}C_c$ SD	$\delta^{18}O_c$	$\delta^{18}O_c$	$\delta^{18}O_c$ SD	Δ_{47}	Δ_{47} SD	Δ_{47} SE	$\delta^{13}C_{ca_{rb}}$	$\delta^{13}C_{bica_{rb}}$	$^{13}\varepsilon$	$\delta^{18}O_w$	$^{18}\alpha$	1000ln α	1000ln α

		(VPDB, ‰)	(VPDB, ‰)	(VPDB, ‰)	(VSMOW, ‰)	(VPDB, ‰)	($CDES_{90}$)	($CDES_{90}$)	($CDES_{90}$)	(VPDB, ‰)	(VPDB, ‰)	(VPDB, ‰)	(VSMOW, ‰)		This Study	vDea18
15-1A	1	-6.48	-	-2.18	27.95	-	0.593	-	-	-7.72	-7.19	0.71	-6.76	1.04	35.1	31.99
15-1C	2	-7.99	0.63	-8.04	21.91	1.01	0.600	0.004	0.003	-7.72	-7.19	-0.8	-7.36	1.03	29.2	31.99
15-2A	3	-6.83	0.07	-3.61	26.48	0.43	0.581	0.022	0.013	-7.72	-7.19	0.36	-6.98	1.03	33.66	31.99
25-1A	1	-7.01	-	-8.93	20.99	-	0.606	-	-	-7.72	-7.19	0.18	-7.45	1.03	28.3	29.7
25-1B	4	-5.91	0.33	-5.91	24.11	0.25	0.580	0.015	0.007	-7.72	-7.19	1.28	-7.4	1.03	31.4	29.7
25-2A	3	-6.16	0.12	-5.69	24.33	0.15	0.555	0.009	0.005	-7.72	-7.19	1.03	-7.26	1.03	31.57	29.7
25-3A	3	-6.56	0.07	-5.91	24.11	0.42	0.558	0.019	0.009	-7.72	-7.19	0.63	-7.19	1.03	31.35	29.7
50-2A	4	-6.76	0.14	-11.7	18.13	0.27	0.497	0.026	0.013	-7.72	-7.19	0.43	-7.07	1.03	24.95	24.6
50-3A	3	-6.83	0.13	-10.93	18.93	0.43	0.522	0.037	0.021	-7.72	-7.19	0.36	-6.31	1.03	26.28	24.6
50-4C	1	-7.32	-	-13.65	16.12	-	0.534	-	-	-7.72	-7.19	-0.13	-6.78	1.02	23.52	24.6
75-1A	3	-6.9	0.05	-12.9	16.89	0.38	0.436	0.011	0.011	-7.72	-7.19	0.29	-4.39	1.02	24.28	20.72
75-2B	4	-6.9	0.11	-15.71	14	0.26	0.452	0.009	0.009	-7.72	-7.19	0.29	-6.65	1.02	21.43	20.72
Jm-Sd-1	6	-9.82	0.16	-13.85	15.92	0.74	0.355	0.020	0.023	-	-	-	-	-	-	-
Jm-Sd-1-625	3	-10.79	0.10	-13.46	16.32	0.03	0.206	0.019	0.006	-	-	-	-	-	-	-

Table 2 (above). Results of isotopic analyses for all experimental precipitates as well as the heated siderite sample (JMP-Sd-1) before and after heating. Here, vDea18 refers to van Dijk et al. (2018).

Experiment	$\delta^{18}O_I$	$\delta^{18}O_I$ (SD)	$\delta^{18}O_F$	$\delta^{18}O_F$ (SD)	$\Delta^{18}O$
DI Control	-7.4	0.07	-7.4	0.07	0.00
15-1A	-6.25	0.06	-7.27	0.02	1.02
15-1C	-7.33	0.02	-7.38	0.01	0.05
15-2A	-6.97	-	-6.99	0.01	0.02
25-1A	-	-	-7.49	0.02	-
25-1B	-	-	-	-	-
25-2A	-	-	-	-	-
25-3A	-	-	-6.97	0.07	-
50-2A	-	-	-6.73	-	-
50-3A	-6.11	0.02	-6.51	0.03	0.4
50-4C	-6.77	0.02	-6.78	0.03	0.01
75-1A	-4.95	0.02	-3.83	0.02	-1.12
75-1B	-6.53	0.02	-6.76	0.02	0.23

Table 3. Results of oxygen isotope analyses of initial (I) and final (F) fluid samples. For samples where the initial oxygen isotope value is 0, initial samples were not available. Fluid samples from experiments 25-1B and 25-2A are not included because no data is available.

Figure Captions

Figure 1. Schematic of reaction vessel used for precipitation experiments. When vacuum grease was used for sealing, a thin layer was applied to the vessel rim and the rim lid before being placed in the glovebox. Each port on the lid was sealed with Parafilm and Teflon tape; 3 ports were sealed around the titrator burettes and the pH electrode. The entire vessel was placed on a magnetic stir plate to facilitate uniform fluid chemistry for the experiment duration. The temperature-controlled fluid inside of the vessel jacket was maintained at a height just below the vessel rim.

Figure 2. Experimental conditions of a well-controlled, sealed experiment (EXPCC25-3A) modeled at 25-75% Fe precipitation as siderite. The duration of this experiment was 27.5 hours from the first $FeCl_2$ titrant injection to experiment termination.

Figure 3. Modeled solution conditions for an experiment with large pH fluctuation, but controlled titrant addition (EXPCC25-1B). Experimental duration was 57.5 hours from the first $FeCl_2$ titrant injection to experiment termination.

Figure 4. Modeled solution conditions in a well-sealed but poorly-controlled experiment (EXPCC75-2B) at 75ºC. Experiment duration was 24 hours from the first $FeCl_2$ titrant injection to experiment termination.

Figure 5. XRD patterns of siderite precipitated at 15, 25, 50, and 75°C.

Figure 6. Comparison of XRD patterns for pure siderite (bottom, EXPCC25-1B) and a siderite/chukanovite mix (top, EXPCC25-1A). Important distinguishing features include the doublet peak at 35° 2θ, which is characteristic of chukanovite, and the noisy background of the chukanovite-bearing pattern.

Figure 7. Modeled Fe speciation and siderite saturation as functions of [DIC] and temperature. Precipitates are color-coded by temperature, with teal representing 15°C, blue representing 25°C, yellow representing 50°C, and pink representing 75°C. Symbols represent individual experiments, with circles denoting experiments in which chukanovite was formed; squares, diamonds, and stars each represent an experiment in which pure siderite was formed, with different shapes used to distinguish between separate experiments conducted at the same temperature.

Figure 8. Results of carbon isotope fractionation (ε) between Fe-carbonate and DIC (HCO_3^-) versus temperature for all precipitates from this study. Our data are plotted against the calculated ε values for calcite from Romanek *et al.* (1992). Chukanovite-bearing samples from this study are marked with a "C". Our siderite samples appear to behave similarly to calcite, though chukanovite is offset to lower epsilon relative to samples of pure siderite.

Figure 9. Regression of temperature versus $1000\ln^{18}\alpha$ for all reported experimental siderite data. The regression is shown in the black line, with the dashed lines representing 95% CL. Error is smaller than the size of the data markers for all samples.

Figure 10. (a) Isotopic results of all measured data plotted with siderite data from Fernandez et al. (2014) and van Dijk et al. (2019). Values from van Dijk et al. (2019) were transferred to $CDES_{90}$ values using an assumed difference in AFF between 90 and 115°C of 0.021‰. This was calculated from the reported 70-115°C difference from van Dijk et al. (2019; 0.043‰) and the 70-90°C difference from Petersen et al. (2019; 0.022‰). Data for natural siderite samples was taken from van Dijk *et al.* 2019. (b) Results of isotopic analyses with the chemostatic experiments highlighted. An experiment is considered to be "sealed" if silicone vacuum grease was applied to the vessel-lid contact. Chukanovite-bearing precipitates are data points marked with a "C". Degree of pH control does not appear to be a major control on predicted equilibrium. For both figures, error bars represent 1 SE.

Figure 11. Comparison of rate of Fe:DIC change for experiments 25-3A (well-controlled, chemostatic), 75-2B (less well-controlled, still chemostatic), and 25-1B (poorly controlled, non-chemostatic).

Figure 12. Regression of all published siderite data (chukanovite-bearing samples from this study excluded from the regression calculation) with an R^2 value of 0.756. Values from van Dijk et al. (2019) were transferred to $CDES_{90}$ values using an assumed difference in AFF between 90 and 115°C of 0.021‰. This was calculated from the reported 70-115°C difference from van Dijk et al. (2019; 0.043‰) and the 70-90°C difference from Petersen et al. (2019; 0.022‰). Error bars are 1 SE.

Figure 13. Δ_{47} vs. $1000\ln^{18}\alpha$ for all Fe-carbonate data normalized to the predicted Δ_{47} and $1000\ln^{18}\alpha$ values of the composite calibrations presented in this study for both parameters and plotted with the expected trends for KIE associated with disequilibrium, including hydration and hydroxylation (Falk *et al*. 2016). The ellipse centered at the origin represents 95% CL associated with predicted equilibrium curves. Error bars shown are from the error on the measurement (1 SE). Chukanovite-bearing samples from this study are marked with a C.

Figures (in order)

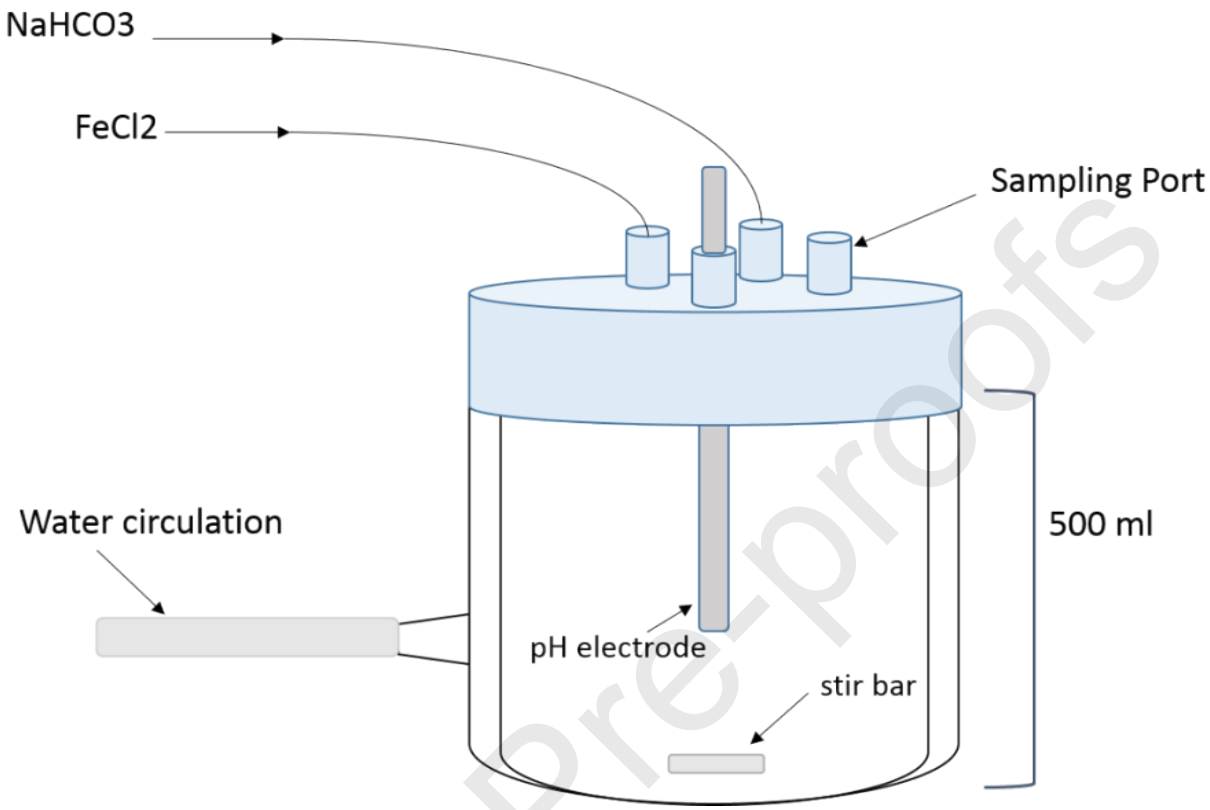

Figure 1

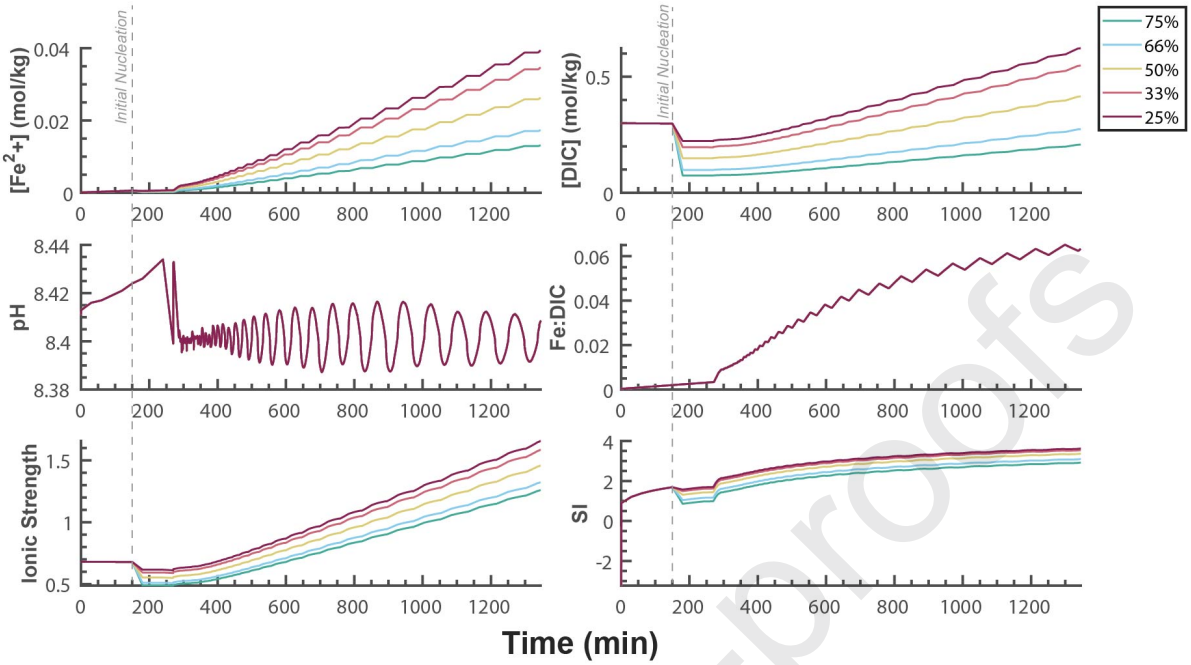

Figure 2 (above), Figure 3 (below)

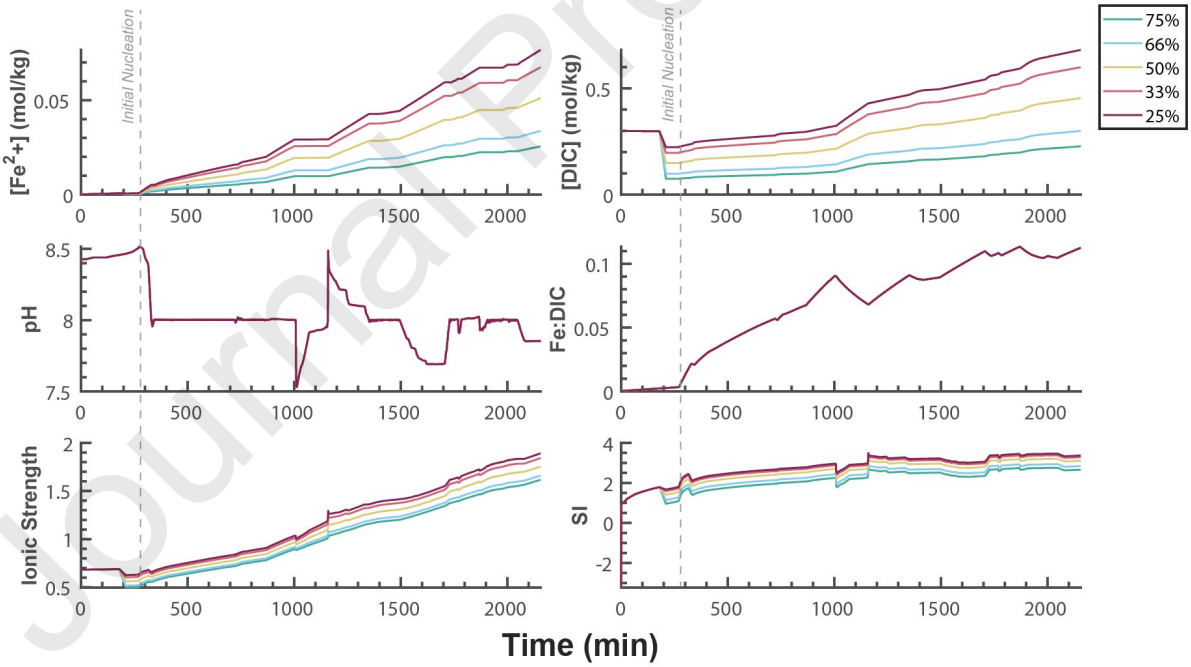

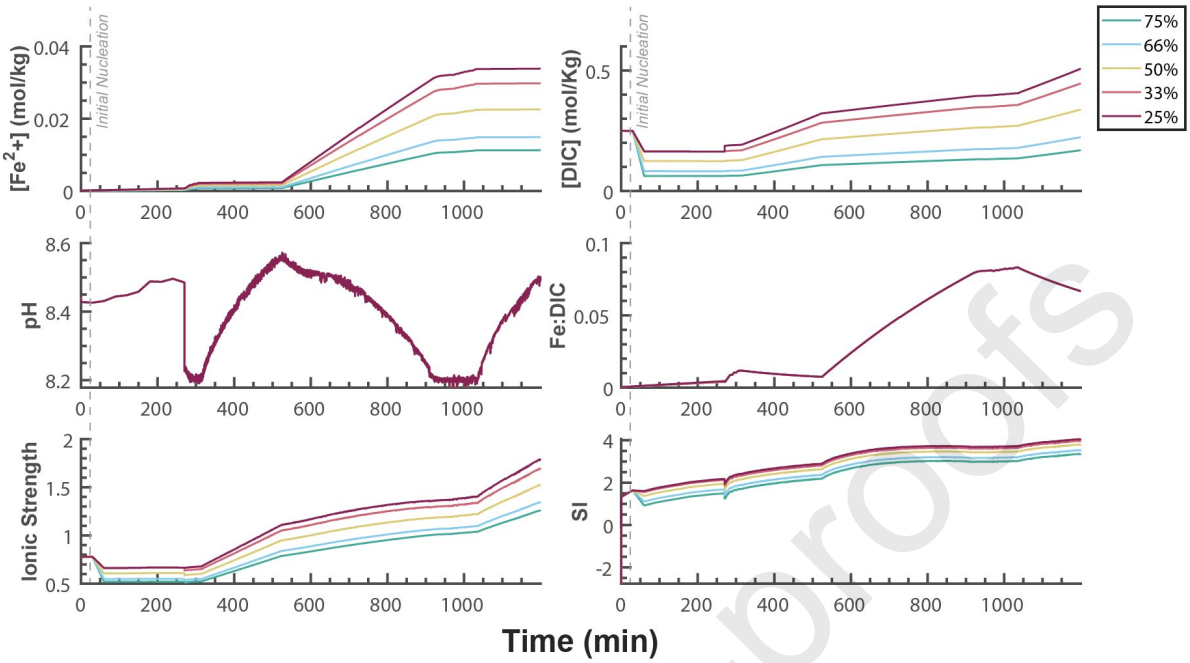

Figure 4 (above), Figure 5 (below)

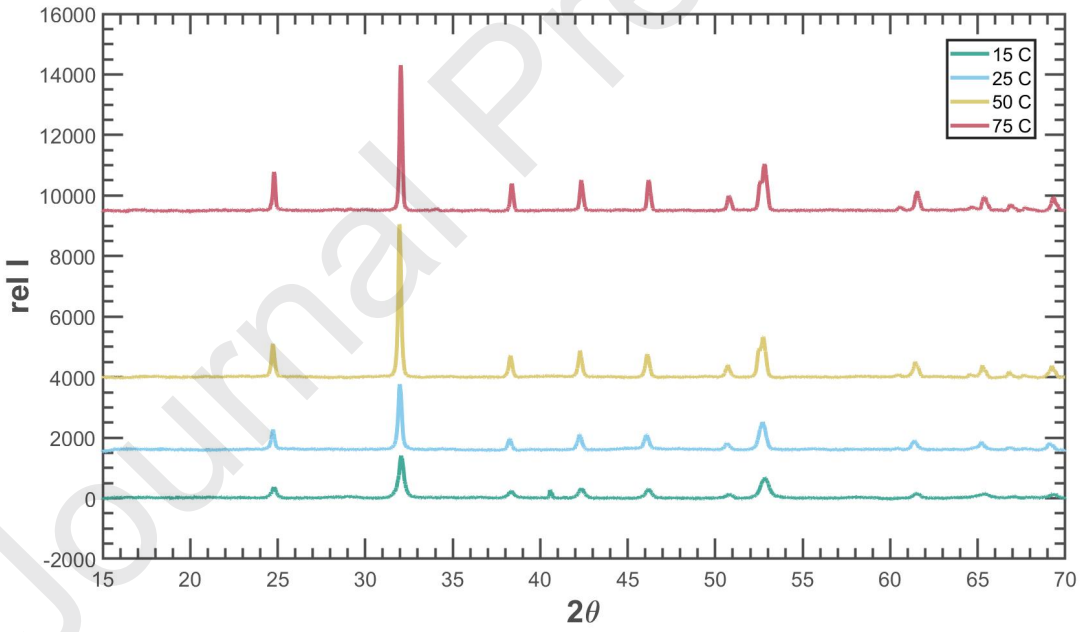

Figure 6 (below)

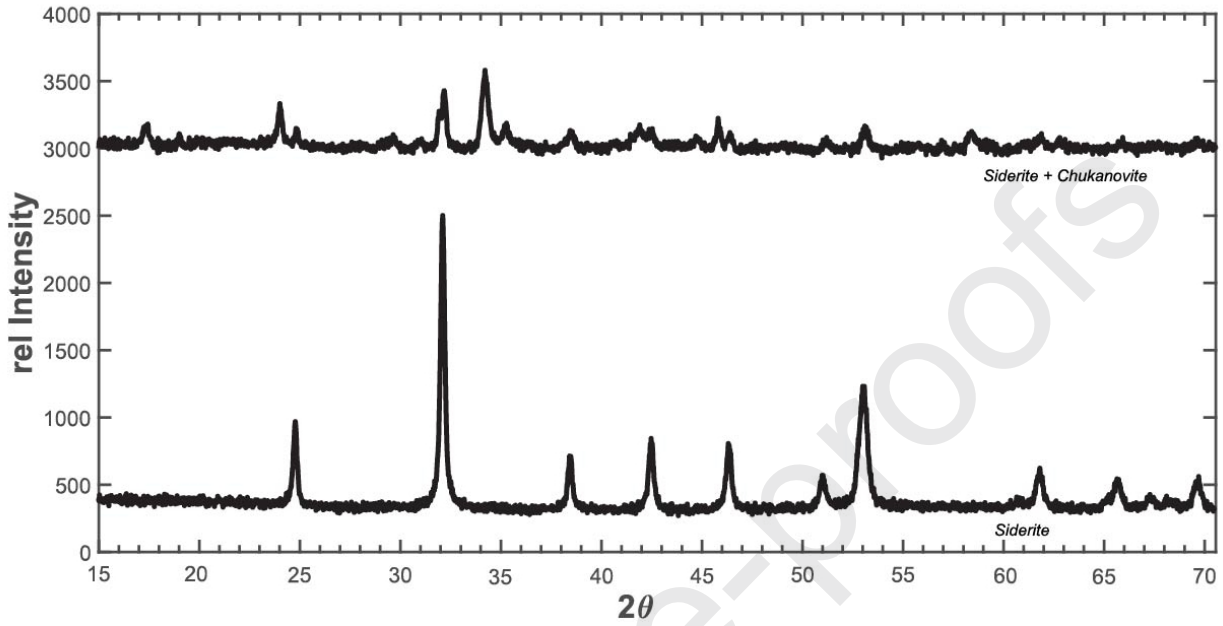

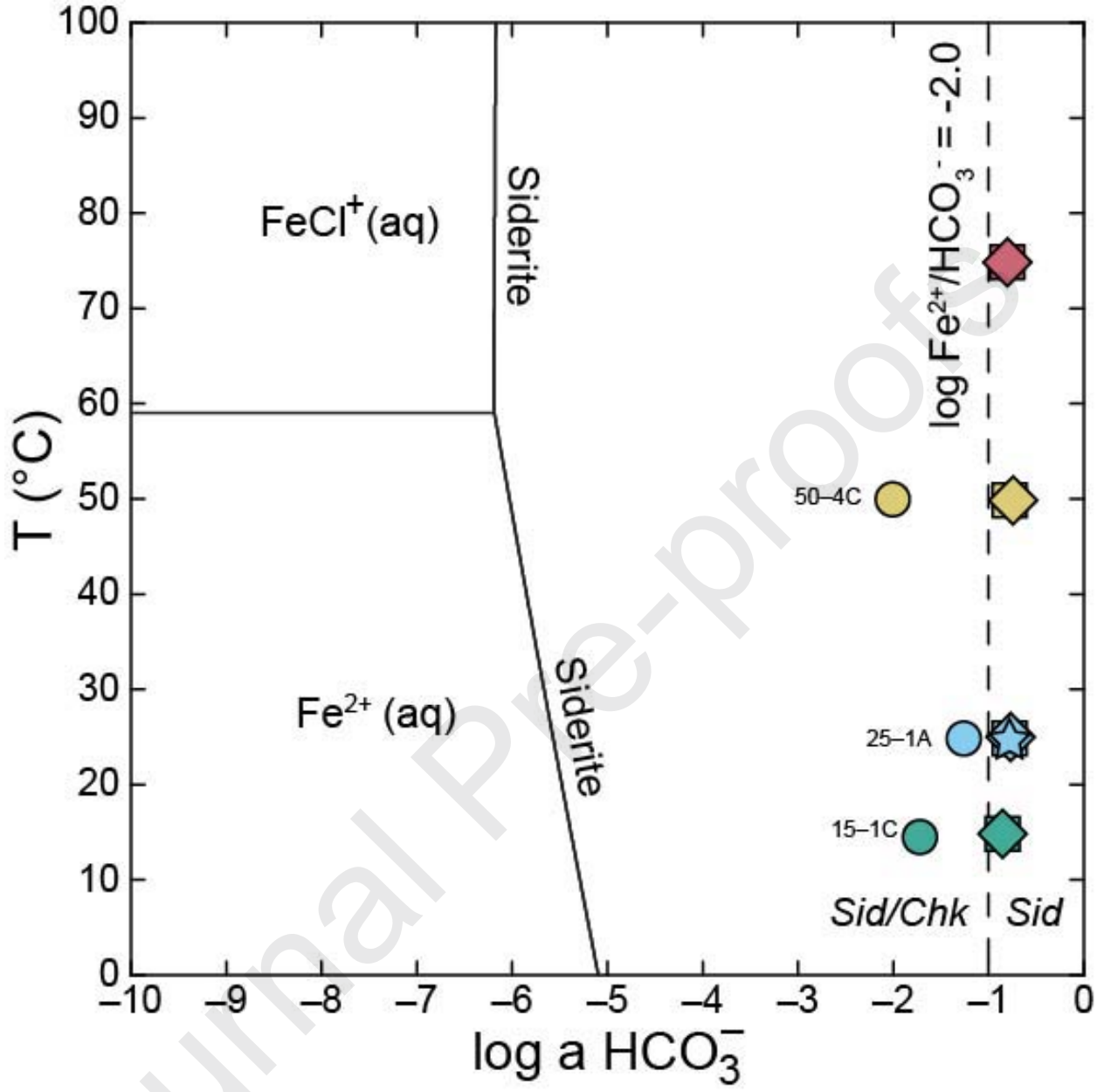

Figure 7

Figure 8 (below)

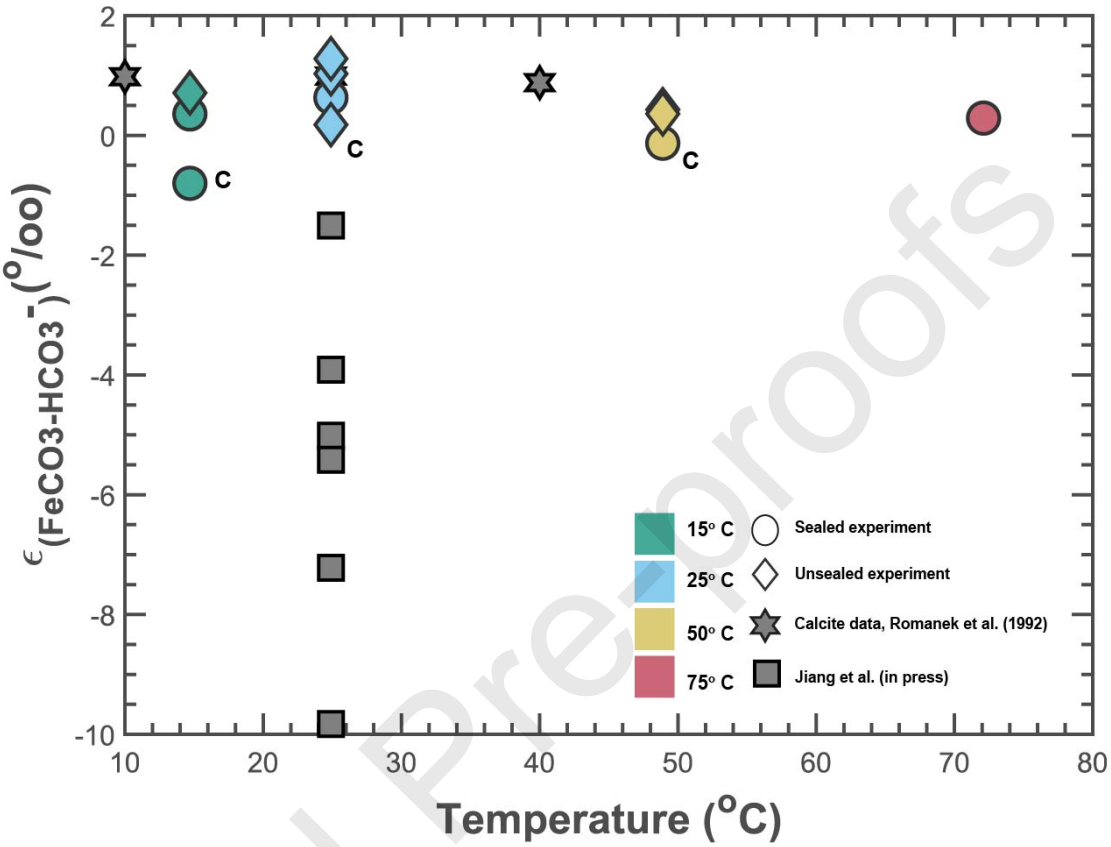

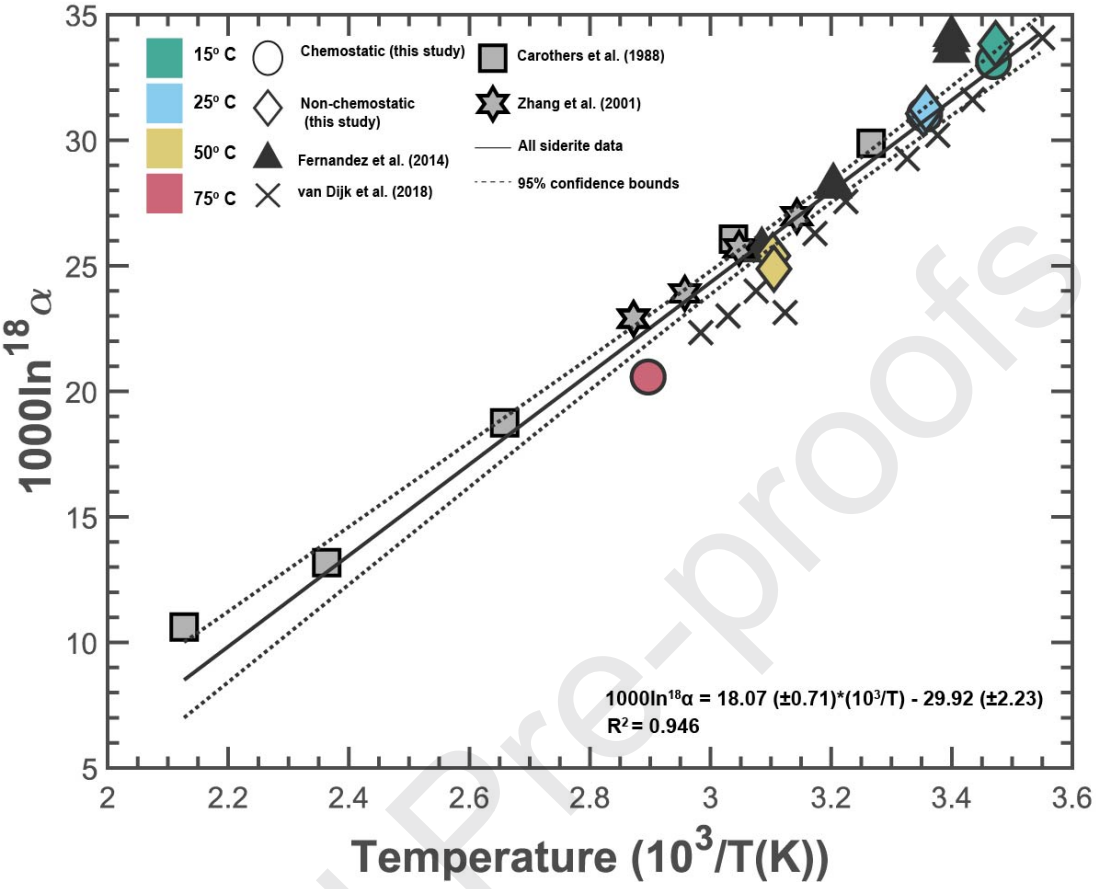

Figure 9

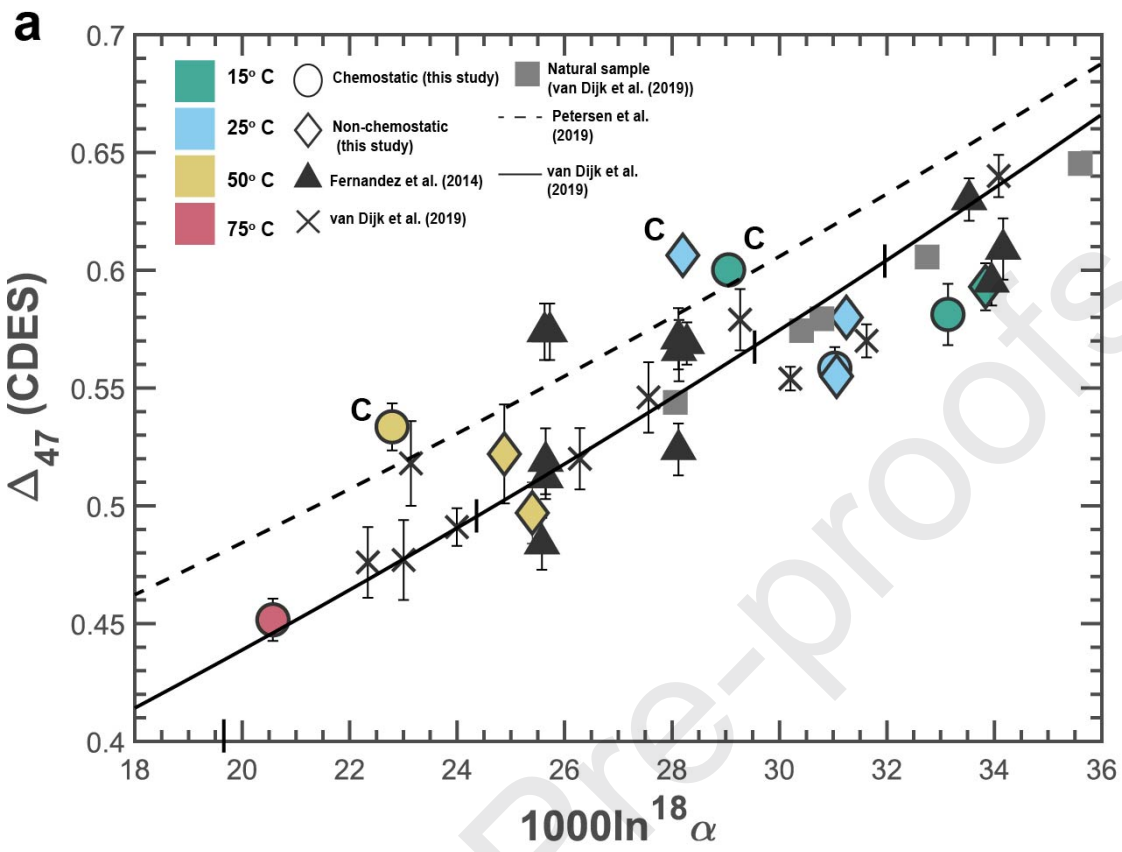

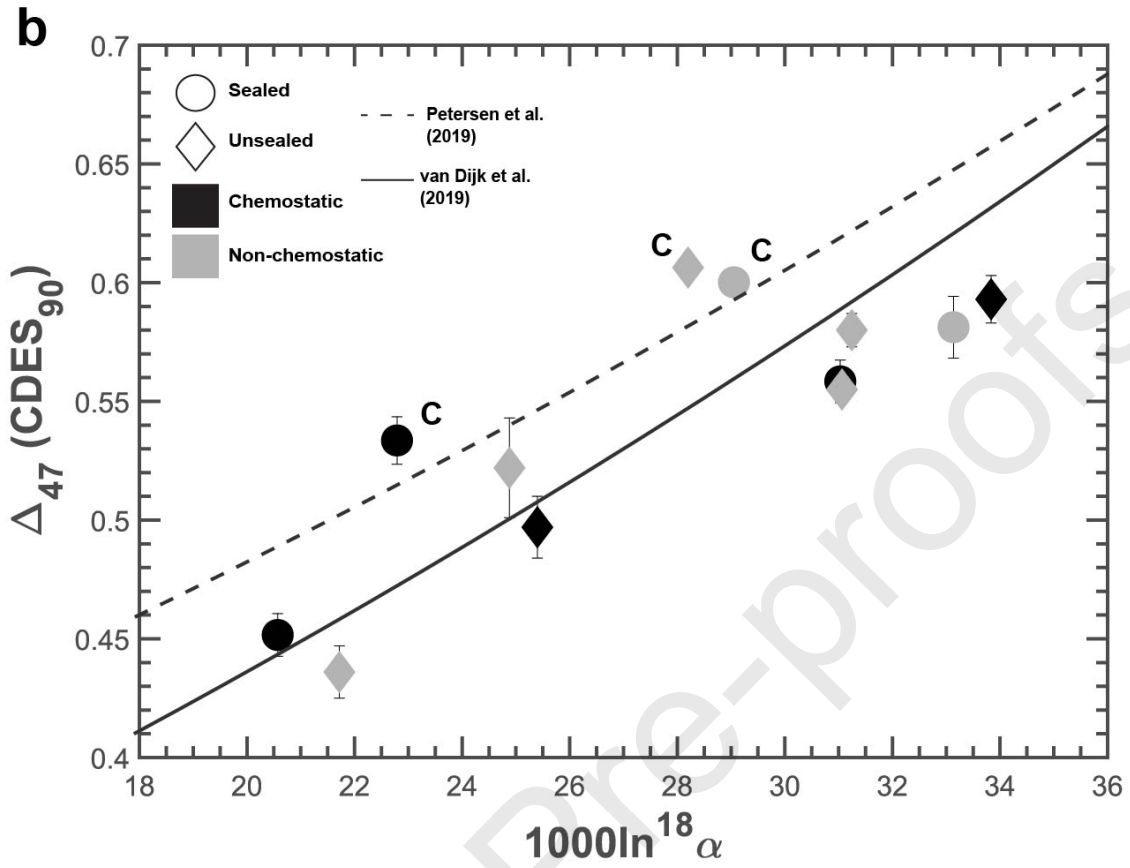

Figure 10 (a, previous page; b, above)

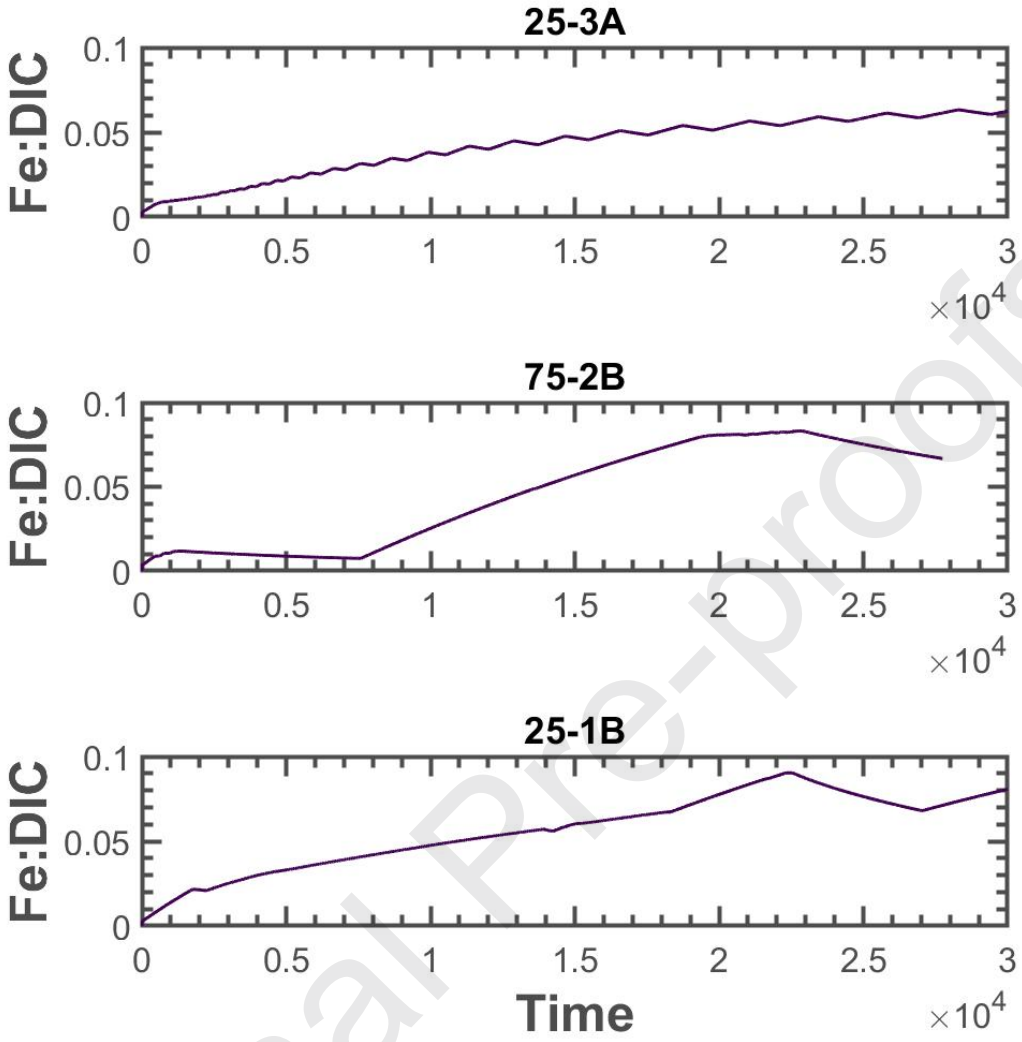

Figure 11

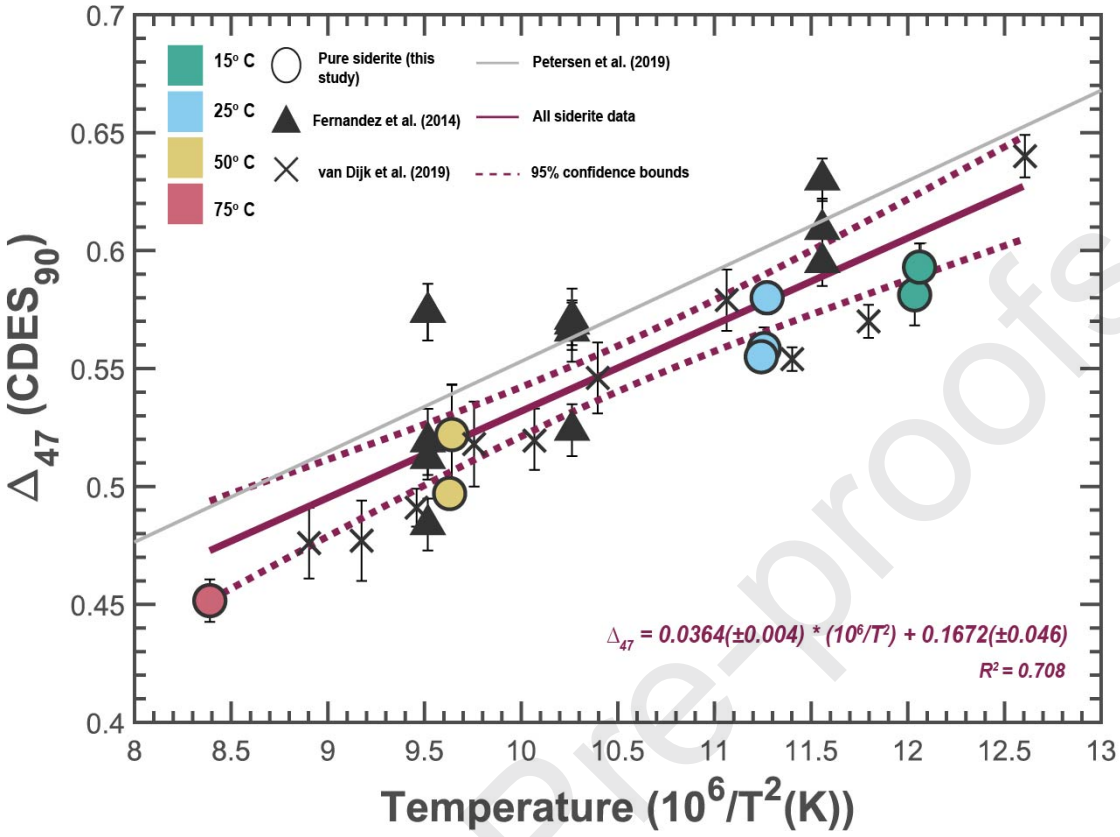

Figure 12

Figure 13 (below)

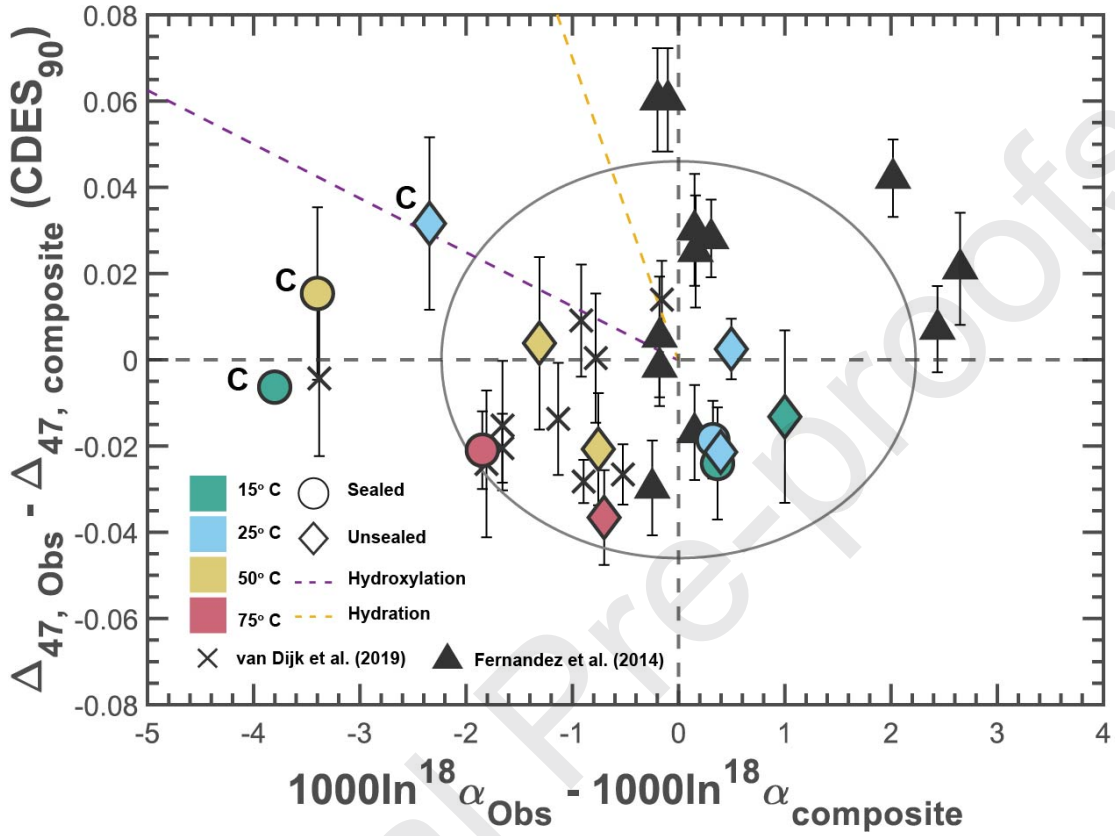

	Other Expt. Conditions				Expt. Target Values					Expt. Observed Values				
Sample	Chemostatic*	Sealed**	Duration (hrs)	Temp	I.S. (M)	Fe (M)	DIC (M)	pH	Fe:DIC	SI	Temp	pH	pH variation	XRD
15-1A	Y	N	24	15	0.485	0.0025	0.25	8.5	0.010	1.390	14.8	8.494-8.578	0.084	Sid
15-1C	N	Y	24	15	0.352	0.0025	0.045	8.8	0.056	1.152	14.7	8.703-8.803	0.1	Sid/Chk
15-2A	Y	Y	24	15	0.485	0.0025	0.25	8.3	0.010	1.709	15.1	8.270-8.315	0.045	Sid
25-1A	N	N	72	25	0.595	0.005	0.1	8.5	0.050	1.746	25.7	8.486-8.632	0.146	Sid/Chk
25-1B	N	N	48	25	0.524	0.001	0.3	8.0	0.003	1.789	24.7	7.530-8.515	0.985	Sid
25-2A	N	N	36	25	0.524	0.001	0.3	8.5	0.003	2.007	25.1	7.994-8.744	0.75	Sid
25-3A	Y	Y	24	25	0.524	0.001	0.3	8.4	0.003	1.690	24.9	8.387-8.434	0.047	Sid
50-2A	N	N	48	50	0.473	0.001	0.3	8.8	0.003	2.105	49.1	8.441-8.881	0.44	Sid
50-3A	N	N	60	50	0.473	0.001	0.3	8.3	0.003	1.629	48.9	7.618-8.307	0.689	Sid
50-4C	Y	Y	48	50	0.422	0.001	0.015	7.9	0.067	0.737	48.9	7.836-7.912	0.076	Sid/Chk
75-1A***	N	N	24	75	0.558	0.001	0.25	8	0.004	1.617	72.1	8.092-8.563	0.471	Sid
75-2B	Y	Y	12	75	0.558	0.001	0.25	8.2	0.004	1.636	72.1	8.178-8.572	0.394	Sid

*Defined has having pH fluctuations of <0.1 units over the course of the experiment

**Defined by the presence or absence of vacuum grease on the vessel-lid contact

***Significant evaporative water losses were observed in this experiment

Sample	Count	$\delta^{13}C_c$ (VPDB, ‰)	$\delta^{13}C_c$ SD (VPDB, ‰)	$\delta^{18}O_c$ (VPDB, ‰)	$\delta^{18}O_c$ (VSMOW, ‰)	$\delta^{18}O_c$ SD (VPDB, ‰)	Δ_{47} ($CDES_{90}$)	Δ_{47} SD ($CDES_{90}$)	Δ_{47} SE ($CDES_{90}$)	$\delta^{13}C_{carb}$ (VPDB, ‰)	$\delta^{13}C_{bicarb}$ (VPDB, ‰)	$^{13}\varepsilon$ (VPDB, ‰)	$\delta^{18}O_w$ (VSMOW, ‰)	$^{18}\alpha$	1000lnα This Study	1000lnα vDea18
15-1A	1	-6.48	-	-2.18	27.95	-	0.593	-	-	-7.72	-7.19	0.71	-6.76	1.04	35.1	31.99
15-1C	2	-7.99	0.63	-8.04	21.91	1.01	0.600	0.004	0.003	-7.72	-7.19	-0.8	-7.36	1.03	29.2	31.99
15-2A	3	-6.83	0.07	-3.61	26.48	0.43	0.581	0.022	0.013	-7.72	-7.19	0.36	-6.98	1.03	33.66	31.99
25-1A	1	-7.01	-	-8.93	20.99	-	0.606	-	-	-7.72	-7.19	0.18	-7.45	1.03	28.3	29.7
25-1B	4	-5.91	0.33	-5.91	24.11	0.25	0.580	0.015	0.007	-7.72	-7.19	1.28	-7.4	1.03	31.4	29.7
25-2A	3	-6.16	0.12	-5.69	24.33	0.15	0.555	0.009	0.005	-7.72	-7.19	1.03	-7.26	1.03	31.57	29.7
25-3A	3	-6.56	0.07	-5.91	24.11	0.42	0.558	0.019	0.009	-7.72	-7.19	0.63	-7.19	1.03	31.35	29.7
50-2A	4	-6.76	0.14	-11.7	18.13	0.27	0.497	0.026	0.013	-7.72	-7.19	0.43	-7.07	1.03	24.95	24.6
50-3A	3	-6.83	0.13	-10.93	18.93	0.43	0.522	0.037	0.021	-7.72	-7.19	0.36	-6.31	1.03	26.28	24.6
50-4C	1	-7.32	-	-13.65	16.12	-	0.534	-	-	-7.72	-7.19	-0.13	-6.78	1.02	23.52	24.6
75-1A	3	-6.9	0.05	-12.9	16.89	0.38	0.436	0.011	0.011	-7.72	-7.19	0.29	-4.39	1.02	24.28	20.72
75-2B	4	-6.9	0.11	-15.71	14	0.26	0.452	0.009	0.009	-7.72	-7.19	0.29	-6.65	1.02	21.43	20.72
Jm-Sd-1	6	-9.82	0.16	-13.85	15.92	0.74	0.355	0.020	0.023	-	-	-	-	-	-	-
Jm-Sd-1-625	3	-10.79	0.10	-13.46	16.32	0.03	0.206	0.019	0.006	-	-	-	-	-	-	-

Experiment	$\delta^{18}O_I$	$\delta^{18}O_I$ (SD)	$\delta^{18}O_F$	$\delta^{18}O_F$ (SD)	$\Delta^{18}O$
DI Control	-7.4	0.07	-7.4	0.07	0.00
15-1A	-6.25	0.06	-7.27	0.02	1.02
15-1C	-7.33	0.02	-7.38	0.01	0.05
15-2A	-6.97	-	-6.99	0.01	0.02
25-1A	-	-	-7.49	0.02	-
25-1B	-	-	-	-	-
25-2A	-	-	-	-	-
25-3A	-	-	-6.97	0.07	-
50-2A	-	-	-6.73	-	-
50-3A	-6.11	0.02	-6.51	0.03	0.4
50-4C	-6.77	0.02	-6.78	0.03	0.01
75-1A	-4.95	0.02	-3.83	0.02	-1.12
75-1B	-6.53	0.02	-6.76	0.02	0.23

Declaration of interests

☒ The authors declare that they have no known competing financial interests or personal relationships that could have appeared to influence the work reported in this paper.

☐The authors declare the following financial interests/personal relationships which may be considered as potential competing interests: